

# Evidence of magnetospheric vacuum birefringence in the polarized X-rays of a radio magnetar

Rachael E. Stewart <sup>1\*†</sup>, Hoa Dinh Thi <sup>2\*†</sup>, George Younes <sup>3,4\*</sup>,  
 Marcus E. Lower <sup>5\*</sup>, Matthew G. Baring <sup>2\*</sup>, Michela Negro <sup>6</sup>,  
 Fernando Camilo <sup>7</sup>, Joel B. Coley <sup>8</sup>, Teruaki Enoto <sup>9</sup>,  
 Alice K. Harding <sup>10</sup>, Wynn C. G. Ho <sup>11</sup>, Chin-Ping Hu <sup>12</sup>,  
 Philip Kaaret <sup>13</sup>, Paul Scholz <sup>14</sup>, Alex Van Kooten <sup>1</sup>,  
 Zorawar Wadiasingh <sup>15,3</sup>

<sup>1</sup>Department of Physics, George Washington University, 725 21st Street NW, Washington DC, 20052, District of Columbia, USA.

<sup>2</sup>Department of Physics and Astronomy, Rice University, 6100 Main Street, Houston, 77251, Texas, USA.

<sup>3</sup>Astrophysics Science Division, NASA Goddard Space Flight Center, 8800 Greenbelt Road, Greenbelt, 20771, Maryland, USA.

<sup>4</sup>Center for Space Sciences and Technology, University of Maryland Baltimore County, 1000 Hilltop Cir, Baltimore County, 21250, Maryland, USA.

<sup>5</sup>Centre for Astrophysics and Supercomputing, Swinburne University of Technology, PO Box 218, Hawthorn, 3122, Victoria, Australia.

<sup>6</sup>Department of Physics and Astronomy, Louisiana State University, 202 Nicholson Hall, Baton Rouge, 70803, Louisiana, USA.

<sup>7</sup>South African Radio Astronomy Observatory, Liesbeek House, River Park, Cape Town, 7700, South Africa.

<sup>8</sup>Department of Physics and Astronomy, Howard University, Washington, DC 20059, USA; CRESST/Mail Code 661, Astroparticle Physics Laboratory, NASA Goddard Space Flight Center, Greenbelt, MD 20771, USA.

<sup>9</sup>Department of Physics, Kyoto University, Kyoto, Japan.

<sup>10</sup>Theoretical Division, Los Alamos National Laboratory, Los Alamos, 87545, New Mexico, USA.

<sup>11</sup>Department of Physics and Astronomy, Haverford College, 370 Lancaster Avenue, Haverford, 19041, Pennsylvania, USA.

<sup>12</sup>Department of Physics, National Changhua University of Education,  
No. 1, Jinde Rd., Changhua, 500207, Taiwan.

<sup>13</sup>NASA Marshall Space Flight Center, Huntsville, 35812, AL, USA.

<sup>14</sup>Department of Physics and Astronomy, York University, 4700 Keele  
Street, Toronto, MJ3 1P3, ON, Canada.

<sup>15</sup>Department of Astronomy, University of Maryland, College Park,  
20742, MD, USA.

\*Corresponding author(s). E-mail(s): [raestewart@gwu.edu](mailto:raestewart@gwu.edu);  
[hoa.dinh@rice.edu](mailto:hoa.dinh@rice.edu); [george.a.younes@nasa.gov](mailto:george.a.younes@nasa.gov); [mlower@swin.edu.au](mailto:mlower@swin.edu.au);  
[baring@rice.edu](mailto:baring@rice.edu);

†These authors contributed equally to this work.

### Summary paragraph

The quantum electrodynamics (QED) theory predicts that the quantum vacuum becomes birefringent in the presence of ultra-strong magnetic fields [1, 2] – a fundamental effect yet to be directly observed. Magnetars, isolated neutron stars with surface fields exceeding  $10^{14}$  G [3], provide unique astrophysical laboratories to probe this elusive prediction [4–6]. Here, we report phase- and energy-resolved X-ray polarization measurements of the radio-emitting magnetar 1E 1547.0–5408 obtained with the Imaging X-ray Polarimetry Explorer (IXPE), in coordination with the Neutron Star Interior Composition Explorer (NICER) and Parkes/Murriyang radio observations. We detect a high phase-averaged polarization degree of 65% at 2 keV, where the surface thermal emission is dominant, rising to nearly 80% at certain rotational phases, and remaining at  $\gtrsim 40\%$  throughout the radio beam crossing. We also observe a strong decrease in polarization from 2 keV to 4 keV. Detailed atmospheric radiative transfer modeling, coupled with geometrical constraints from radio polarization, demonstrate that the observed polarization behavior cannot be consistently explained without invoking magnetospheric vacuum birefringence (VB) influences. These observational findings combined with theoretical simulations provide evidence for quantum VB naturally occurring in magnetar magnetospheres. This work marks a significant advance toward confirming this hallmark prediction of QED and lays the foundation for future tests of strong-field quantum physics using next-generation X-ray polarimeters.

Magnetars [3, 7, 8], a class of isolated neutron stars (NS), possess the strongest known magnetic fields in the observable universe ( $B_{\text{surface}} \sim 10^{14-15}$  G), surpassing the typical field strength of young, rotation-powered pulsars by 1–3 orders of magnitude. The decay of these magnetic fields powers persistent, high-luminosity X-ray emission, which typically peaks between 0.5 keV and 10 keV and reaches  $L_X \gtrsim 10^{35}$  erg s<sup>-1</sup> (see e.g. [9] for a review). With magnetic field strengths that far exceed the quantum electrodynamic (QED) critical field  $B_{\text{cr}} = 4.4 \times 10^{13}$  G, magnetars are widely recognized as promising astrophysical laboratories for testing exotic, non-linear QED processes in the strong B-field regime [10, 11].

One such prediction is vacuum birefringence (VB), wherein intense magnetic fields – comparable to those of magnetars – substantially modify the refractive indices of photon polarization eigenmodes and render them disparate: different polarizations propagate at different speeds [12, 13]. This property is a direct consequence of the polarization of the quantum vacuum, and its constituent “virtual” electron-positron pairs, by the electromagnetic field [1, 2], and remains an unverified prediction of QED. Although indirect evidence consistent with the action of VB has been reported both in laboratory contexts [14] and in astrophysical settings [15–17], direct, unambiguous measurements of VB in either of these settings has remained elusive [11, 15, 18–20]. Together, these complementary approaches offer promising paths to a decisive confirmation of one of the most exotic predictions of QED.

The influence of VB in magnetar magnetospheres is expected to strongly enhance the polarization signature of soft X-ray photons emerging from their surfaces. These photons are predicted to undergo differential phase shifts depending on their two polarization modes – ordinary (O mode) and extraordinary (X mode). If  $\mathbf{k}$  represents a photon’s momentum vector, the O mode ( $\parallel$ ) has an electric field vector approximately in the  $\mathbf{k}$  -  $\mathbf{B}$  plane, and the X mode ( $\perp$ ) has its electric field perpendicular to this plane. This phenomenon decouples the polarization eigenmodes out to altitudes of  $\sim 30 - 300$  stellar radii [21], leading to a tight correlation of their polarization vectors with the magnetospheric field morphology. The result is that VB enhances the net linear polarization of surface emission, potentially producing polarization degrees (PDs) approaching 100% under ideal viewing geometries [5, 21, 22]. Inside magnetar atmospheres, the combined influence of vacuum and plasma birefringence allows photons to convert between polarization modes [4, 20]. This mode conversion is most efficient at a QED vacuum resonance (VR) energy (typically around a few keV) that depends on the hydrogenic plasma density, the local field strength and light propagation direction, and acts to depolarize the net PD emerging from the surface. Consequently, one expects a rotational-phase-averaged high PD away from the VR energy and significant PD reduction near it due to increased mode mixing.

1E 1547.0–5408 is a canonical magnetar with a spin period of 2.09 s and a surface equatorial magnetic field strength of  $\approx 2.2 \times 10^{14}$  G [23]. It is currently in a persistently bright X-ray state, exhibiting a typical magnetar spectrum – a soft thermal-like component prominent in the  $\lesssim 10$  keV band, and a hard X-ray tail dominating at higher energies [24, 25]. The broadband 0.5–70 keV spectrum is best fit with either a double blackbody (BB) thermal contribution and a non-thermal power-law (PL) model or a single BB and double PL model [24, 25]. The pulse shape at all energies is virtually

sinusoidal, with minimal contribution from higher harmonics. The root-mean-squared (RMS) pulsed fraction [26] is notably large compared to the rest of the magnetar population – it also exhibits a strong energy-dependence with a value of  $\sim 30\%$  at 2 keV that steadily increases to 42% around 6 keV, before decreasing monotonically towards 20% at energies  $> 10$  keV [24, 25]. These spectral+timing characteristics likely indicate the presence of a thermal hot spot on the surface dominating the softest energies of the spectrum up to  $\sim 6$  keV, whereafter emission of magnetospheric origin overtakes the spectrum’s surface contribution and alters the pulse properties [24, 25].

1E 1547.0–5408 is also unique among the magnetar population as a persistent radio pulsar [27]. It emits broad radio pulses at the spin-period of the magnetar, spanning approximately 25% of the source duty cycle (Methods), unusually wide among the young, isolated NS population. The pulses are also highly polarized and display a characteristic S-shaped swing in the linear polarization position angle [27], indicative of the viewing line-of-sight crossing the radio emission cone [28]. These properties hint at a nearly-aligned rotator, with an observer line-of-sight at a small angle to the rotation axis that samples open magnetic field lines proximate to the polar cap (Methods).

This richness of information offered by the combined X-ray + radio data motivated a deep simultaneous observing campaign with the Imaging X-ray Polarimetry Explorer (IXPE), the Neutron star Interior Composition ExploreR (NICER), and *Murriyang*, the 64 m Parkes radio telescope, which was carried out between March 26, 2025 UTC 03:01:52 and April 5, 2025 UTC 00:26:53. Our ultimate goal is to study in detail the soft (2–8 keV) X-ray polarimetric properties of the source as afforded by IXPE and to place it in context of the geometrical constraints achievable through the radio observations. Hence, all of the observations were coordinated to optimize simultaneous coverage between the instruments, particularly with IXPE (see Methods for full details of the observations).

The IXPE data reveal an energy and phase-averaged 2–8 keV PD of about  $46 \pm 4\%$  ( $1\sigma$  uncertainty; here and throughout the rest of the text) with a polarization angle (PA) of  $-76^\circ \pm 3^\circ$  (Figure 1) with a statistical significance of  $\sim 10.5\sigma$  above the minimum detectable polarization value for the 99% confidence level ( $\text{MDP}_{99}$ ). This is the largest such PD in the population of six IXPE-observed magnetars [11, 29, 30]. The PD also displays strong energy dependence, achieving a maximum at  $59 \pm 5\%$  in the softest energy band of 2–3 keV before decreasing to  $37 \pm 5\%$  in the 3–4 keV range. The PA of the two bands, on the other hand, remain consistent with that of the energy-integrated measurement. In the hard part of the energy range (4–8 keV), we measure a PD of  $40 \pm 11\%$ , and slightly shifted PA of  $-86^\circ \pm 8^\circ$ , a detection at only the  $3.5\sigma$  significance level, mainly due to its lower signal-to-noise. Notably, the PD of the softest energy range is at least a factor of 2.5 larger than the corresponding values measured in the rest of the population [30].

Using a phase-coherent timing ephemeris that covers our full observing campaign, we phase-fold the X-ray (intensity and polarization) and radio data, after correcting for propagation through the ionized interstellar medium to ensure absolute alignment between the two wavelengths (see Methods). The PD is most prominent in the softer part of the spectrum (Figure 2). It modulates moderately with phase, reaching a peak of  $74 \pm 11\%$  in the 2–4 keV range and a minimum of about  $34 \pm 8\%$ ; the former occurs

close to the X-ray pulse minimum and away from the radio pulse, in contrast to the latter. Note that the PD reaches  $82 \pm 15\%$  in the 2–3 keV range and a minimum of  $42 \pm 12\%$ : see Extended Figure 9. The PA displays a sinusoidal modulation between a maximum of  $-51^\circ \pm 6^\circ$  and a minimum of  $-97^\circ \pm 9^\circ$ . The latter occurs around the minimum radio PA which also reaches similar values.

Finally, the spectro-polarimetric analysis of the IXPE+NICER phase-averaged spectrum reveals that the emission in the soft 1–8 keV X-ray band is best described by a BB component with a temperature  $kT = 0.72 \pm 0.01$  keV and a relatively small emitting area  $R^2 = 1.07 \pm 0.05$  km<sup>2</sup> (see Methods), assuming a source distance of 4.5 kpc [31]. In accentuating the model-independent polarization results presented above, we find that the phase-averaged BB polarization Q and U spectra are best modeled by a linearly decreasing PD from  $65 \pm 8\%$  at 2 keV at a rate of  $-15 \pm 2\%$  keV<sup>-1</sup>, and a constant PA of  $-67^\circ \pm 4^\circ$ . We do not find evidence for any trend of changing PA or PD at the upper-end of the IXPE energy band ( $\gtrsim 4$  keV), as hinted at (albeit at a low significance) in our model-independent analysis. This is likely due to the fact that the 2–8 keV IXPE source spectrum is heavily dominated by the 2–4 keV range where the source is most prominently detected; indeed, adding a second component to the spectrum is not statistically justified, and, when included, remains unconstrained (see Methods).

The modest phase-averaged PD measured for most magnetars in the soft, 2–3 keV X-ray band [ $\lesssim 20\%$ , 30] have so far been interpreted as a sign for the presence of a condensed surface [17, 32]. The much higher PD we measure nominally argues against such a scenario in 1E 1547.0–5408. Indeed, given the high surface temperature reported here and elsewhere [24, 25] and typical dipole magnetic field strength, a magnetic condensation is unlikely for 1E 1547.0–5408 [33]. Phase-averaged polarization degrees approaching 40% may be attainable in a pure magnetized atmosphere without any QED corrections, but obtaining PDs of  $\approx 65\%$  would be nontrivial [6]. More problematic for a magnetized atmosphere are the extreme phase-resolved PDs ( $\approx 70$ –80% in the 2–4 keV band: see Figure 2) and the absence of strong depolarization near the radio pulse phase. Nominally, considerable net X-ray depolarization should arise when sampling polar open field lines [34] during the radio beam crossing (discussed below). Yet, while we indeed detect a minimum X-ray PD during the radio pulse, it is still highly polarized at  $\approx 30$ –40%. The action of VB in 1E 1547.0–5408 naturally addresses these inconsistencies: it both enhances the intrinsic PD and suppresses mode mixing, limiting X-ray depolarization along open field lines and preserving polarization signatures beyond the light cylinder [20].

The decrease in PD within the narrow energy range of 2–4 keV is notable. A separate, and differently polarized component contributing to the BB emission is not evident in the spectral and timing properties of the source which argue for the same thermal component dominating these energies. This behavior is most naturally attributed to mode conversion close to VR [4, 20]. Given the B-field strength of 1E 1547.0–5408, and assuming a hydrogen atmosphere, mode conversion [33] becomes efficient at energies  $\gtrsim 2$  keV. At energies  $\gtrsim 4$  keV, the interpretation becomes less robust due to the reduced signal-to-noise ratio. Nevertheless, the 4–8 keV (and 4–5 keV;

see Methods) band shows a tentative deviation from the trend observed at lower energies. Deeper IXPE observations will be essential to clarify the polarimetric behavior in this regime.

We tested our qualitative picture presented above with detailed modeling of the radio and X-ray pulse and polarization properties. The observed S-shaped sweep of the radio PA across the time and frequency averaged 2.5–4.0 GHz profile in Figure 2 (top) is consistent with the rotating vector model (RVM) for a pure dipolar field geometry [35]. We recover a magnetic and spin axes that are offset by only  $\alpha = 3.4^{+1.3}_{-1.2}$ , along with the angle between the spin axis and our line of sight of  $\zeta = 7.5^{+3.0}_{-2.6}$  (see Figure 1 in [36] for an illustration of these angles); this constitutes an aligned rotator viewed close to the spin axis. Under the simplifying assumption that the open field lines above the polar cap are fully illuminated, this combination of the magnetic and viewing geometry along with the high pulse duty cycle suggest the radio emission originates around  $692^{+654}_{-400}$  km above the NS surface (Methods). This height is less than 1% of the light cylinder, and thus the absolute radio pulse phase accurately describes a magnetic pole crossing. We can combine these constraints on the geometry with detailed modeling of the X-ray intensity, Stokes  $Q/I$ , and  $U/I$  profiles using the atmospheric, magnetized radiative transfer Monte Carlo simulation, *MAGTHOMSCATT* [34, 37, 38], to interpret the IXPE measurements.

For the modeling of X-ray pulsations, we considered various single hot spot scenarios; see Methods for details and  $\chi^2$  values. General relativistic [36] and VB influences (polarization mode decoupling at low to moderate altitudes) on the magnetospheric propagation of polarized light from the stellar surface to a distant observer are treated in our present, upgraded *MAGTHOMSCATT* simulation. The implementation of the VB modifications to magnetospheric propagation is detailed in [38], and VB influences can be routinely switched on and off. This code does not yet include mode conversion at the VR [4] that arises at higher densities with hotter gas deeper in the stratified atmosphere. Thus, we limited our comparisons to the 2–3 keV data, sampling photons that mostly originate from the cooler outer atmospheric layers where the VR effect is expected to be less influential. For a fully comprehensive demonstration of VB in action, scoping beyond our magnetospheric focus, a study including VR modifications to atmospheric polarization configurations is requisite. This would then need to address the energy dependence of the net polarization observed from extended surface regions, a future task that would require greater statistical precision in the polarization data than is afforded by the present observations. We note that even if VR is included in the atmosphere, if VB is switched off in the magnetosphere, strong phase-dependent oscillations in  $Q$  and  $U$  (discussed below) will still result due to summing over the wide variation of field directions on the surface. Accordingly, we expect that the same conclusion of the need for VB in the magnetosphere will be drawn.

Among all the cases considered, the best fit to the intensity ( $\chi^2/\text{dof} = 33.9/30$ ), Stokes  $Q/I$  ( $\chi^2/\text{dof} = 19.0/4$ ), and  $U/I$  ( $\chi^2/\text{dof} = 10.9/4$ ) data correspond to a wedged-shaped hot spot spanning from the magnetic pole to  $17^\circ$  in colatitude and covering  $120^\circ$  in longitude abutting the meridional plane on one side (see the blue region in Figure 11), and the optimal geometry was provided by an  $\alpha = 0^\circ$  and  $\zeta = 1.5^\circ$ . This best fit includes magnetospheric VB influences: see Figure 3 (panels a-c) and the blue

curves therein. These parameters approximately support the aligned rotator geometry revealed by the radio intensity and the radio RVM. We note that the dominant contribution to the  $\chi^2$  values in the fits of Q and U comes from the 7th phase bin at phase  $\phi = 0.875$ , which is only slightly above the 99% MDP (see Methods).

Alternatively, a circular offset hot spot of radius  $\theta_{\text{cap}} = 10^\circ$  (see the green region in Figure 11) with its center located at colatitude  $\theta_c = 17.5^\circ$  and longitude  $\phi_c = 180^\circ$  (see Extended Figure 12, bottom row) with  $(\alpha, \zeta) = (2^\circ, 5.5^\circ)$  produces an acceptable fit to the intensity while matching our constraints on the magnetic and viewing geometry from the radio polarization. However, the pulsation traces of both  $Q/I$  and  $U/I$  in this case do not match the data well.

As shown by Figure 3, in the absence of VB (orange solid curves) the  $Q/I$  (panel b,  $\chi^2/\text{dof} = 106.8/4$ ) and  $U/I$  (panel c,  $\chi^2/\text{dof} = 95.6/4$ ) traces show strong oscillations, a consequence of the convolution of magnetic field directions on the stellar surface. The overall fit quality improves dramatically with the inclusion of VB (blue solid curves) for both the wedge and the circular hot spot scenarios (see also Figure 12). The Q-U representations of these results (panel d, Figure 3) clearly highlight this improvement. Indeed, while the VB-on model (blue) satisfactorily reproduces the observed data, the VB-off one (orange) deviates significantly. We also show in panel (d) the best result among the VB-off models (red), which corresponds to a pole-centered circular hot spot (see Methods for details), and it is evident that the Q and U magnitudes are underestimated in this case. This inference of the likely action of VB in the magnetosphere does not depend on which polarization eigenmode emerges in dominance from the atmosphere, just that one mode is in fact dominant. In addition, we verified that the observed X-ray PA can be successfully fit with a RVM, and the best-fit geometric parameters are broadly consistent with those obtained from the radio analysis (see Methods and Figure 10). This indicates that the X-ray PA data can be described as a purely geometrical effect, a signature of mode-locking due to VB at altitudes up to the polarization limiting radius.

It is notable that for both the optimal wedge solution and the offset circular zone model, the centroids for the X-ray hot spots are at longitudes ( $60^\circ$  for the wedge) substantially removed from the meridional plane containing the rotation and magnetic axes (zero longitude), which serves as the central plane of symmetry for the radio RVM model (one draws a similar conclusion when comparing the radio and X-ray RVM best-fit solutions which imply a  $\Delta\phi_0 \approx 80^\circ$ ; Figure 10). This naturally delivers a phase lag of the X-ray pulse peak relative to the radio pulse that is broadly consistent with that evinced in Figure 2. The dipolar field lines defining the magnetic flux tube that anchors the radio beam nominally thread the surface only near the periphery of the X-ray hot spots. For the surface footpoints of this radio flux tube to be approximately coincident with the X-ray centroids would require a strong non-poloidal field line shear that would be broadly commensurate with the popular paradigm of field twists in magnetars [39, 40]. These field geometry distortions will rotate the net PA somewhat. Yet in the absence of VB, the strong oscillations of Stokes parameters will still persist. Accordingly, the presence of field twists will not enable the phase-resolved data to be explained without invoking the action of VB in the magnetosphere.

The combined insights from these unique X-ray and radio observational results and the theoretical modeling present the most compelling indication of naturally-occurring VB in an astrophysical setting to date, specifically arising in the magnetosphere of 1E 1547.0–5408. These results principally include phase-averaged polarization degrees reaching  $65 \pm 8\%$  at 2 keV, rising to  $82 \pm 15\%$  at certain rotational phases, and the absence of significant depolarization during the radio pulse. The observed substantial decrease in polarization between 2–4 keV is also qualitatively consistent with the expected influence of VR. If the actual phase-averaged polarization degree in 1E 1547.0–5408 exceeds 80% between 0.5–1 keV, as suggested by our spectropolarimetric modeling, the presence of VB affecting magnetar surface emissions would be observationally definitive. Future X-ray polarimetric missions such as GoSOX [41] will be essential for accessing this very soft X-ray domain. Together with laboratory and collider-based efforts, and more extensive observations by IXPE, such initiatives will complete the multi-pronged experimental campaign to directly verify one of the most fundamental predictions of quantum electrodynamics.

## References

- [1] Heisenberg, W. & Euler, H. Folgerungen aus der Diracschen Theorie des Positrons. *Zeitschrift fur Physik* **98**, 714–732 (1936).
- [2] Schwinger, J. On Gauge Invariance and Vacuum Polarization. *Physical Review* **82**, 664–679 (1951).
- [3] Kouveliotou, C. *et al.* An X-ray pulsar with a superstrong magnetic field in the soft  $\gamma$ -ray repeater SGR1806 - 20. *Nature* **393**, 235–237 (1998).
- [4] Lai, D. & Ho, W. C. Polarized X-Ray Emission from Magnetized Neutron Stars: Signature of Strong-Field Vacuum Polarization. *Physical Review Letters* **91**, 071101 (2003).
- [5] van Adelsberg, M. & Perna, R. Soft X-ray polarization in thermal magnetar emission. *MNRAS* **399**, 1523–1533 (2009).
- [6] Taverna, R., Turolla, R., Suleimanov, V., Potekhin, A. Y. & Zane, S. X-ray spectra and polarization from magnetar candidates. *MNRAS* **492**, 5057–5074 (2020).
- [7] Duncan, R. C. & Thompson, C. Formation of very strongly magnetized neutron stars - Implications for gamma-ray bursts. *ApJL* **392**, L9–L13 (1992).
- [8] Paczynski, B. GB 790305 as a very strongly magnetized neutron star. *actaa* **42**, 145–153 (1992).
- [9] Kaspi, V. M. & Beloborodov, A. M. Magnetars. *Annual Review of Astronomy and Astrophysics* **55**, 261–301 (2017).

- [10] Harding, A. K. & Lai, D. Physics of strongly magnetized neutron stars. *Reports on Progress in Physics* **69**, 2631–2708 (2006).
- [11] Taverna, R. & Turolla, R. X-ray Polarization from Magnetar Sources. *Galaxies* **12**, 6 (2024).
- [12] Adler, S. L. Photon splitting and photon dispersion in a strong magnetic field. *Annals of Physics* **67**, 599–647 (1971).
- [13] Tsai, W.-Y. & Erber, T. Propagation of photons in homogeneous magnetic fields: Index of refraction. *Physical Review D* **12**, 1132–1137 (1975).
- [14] Adam, J. *et al.* Measurement of  $e^+e^-$  Momentum and Angular Distributions from Linearly Polarized Photon Collisions. *Physical Review Letters* **127**, 052302 (2021).
- [15] Ho, W. C. G., Lai, D., Potekhin, A. Y. & Chabrier, G. Atmospheres and Spectra of Strongly Magnetized Neutron Stars. III. Partially Ionized Hydrogen Models. *ApJ* **599**, 1293–1301 (2003).
- [16] Mignani, R. P. *et al.* Evidence for vacuum birefringence from the first optical-polarimetry measurement of the isolated neutron star RX J1856.5-3754. *MNRAS* **465**, 492–500 (2017).
- [17] Taverna, R. *et al.* Polarized x-rays from a magnetar. *Science* **378**, 646–650 (2022).
- [18] Ho, W. C. G. & Lai, D. Atmospheres and spectra of strongly magnetized neutron stars - II. The effect of vacuum polarization. *MNRAS* **338**, 233–252 (2003).
- [19] Ejlli, A. *et al.* The PVLAS experiment: A 25 year effort to measure vacuum magnetic birefringence. *Physics Reports* **871**, 1–74 (2020).
- [20] Lai, D. IXPE detection of polarized X-rays from magnetars and photon mode conversion at QED vacuum resonance. *Proceedings of the National Academy of Science* **120**, e2216534120 (2023).
- [21] Heyl, J. S., Shaviv, N. J. & Lloyd, D. The high-energy polarization-limiting radius of neutron star magnetospheres - I. Slowly rotating neutron stars. *MNRAS* **342**, 134–144 (2003).
- [22] Heyl, J. S. & Shaviv, N. J. Polarization evolution in strong magnetic fields. *MNRAS* **311**, 555–564 (2000).
- [23] Camilo, F., Ransom, S. M., Halpern, J. P. & Reynolds, J. 1E 1547.0-5408: A Radio-emitting Magnetar with a Rotation Period of 2 Seconds. *ApJL* **666**, L93–L96 (2007).
- [24] Coti Zelati, F. *et al.* The long-term enhanced brightness of the magnetar 1E

- 1547.0-5408. *A&A* **633**, A31 (2020).
- [25] Lower, M. E. *et al.* The 2022 High-energy Outburst and Radio Disappearing Act of the Magnetar 1E 1547.0-5408. *ApJ* **945**, 153 (2023).
- [26] Bildsten, L. *et al.* Observations of Accreting Pulsars. *ApJs* **113**, 367–408 (1997).
- [27] Camilo, F., Reynolds, J., Johnston, S., Halpern, J. P. & Ransom, S. M. The Magnetar 1E 1547.0-5408: Radio Spectrum, Polarimetry, and Timing. *ApJ* **679**, 681–686 (2008).
- [28] Zeng, S., Philippov, A., Juno, J., Beloborodov, A. M. & Popova, E. Origin of Pulsed Radio Emission from Magnetars. *ApJL* **996**, L20 (2026).
- [29] Stewart, R. *et al.* X-Ray Polarization of the Magnetar 1E 1841-045. *ApJL* **985**, L35 (2025).
- [30] Rigoselli, M. *et al.* IXPE Detection of Highly Polarized X-Rays from the Magnetar 1E 1841-045. *ApJL* **985**, L34 (2025).
- [31] Tiengo, A. *et al.* The Dust-scattering X-ray Rings of the Anomalous X-ray Pulsar 1E 1547.0-5408. *ApJ* **710**, 227–235 (2010).
- [32] Heyl, J. *et al.* The detection of polarized X-ray emission from the magnetar 1E 2259+586. *MNRAS* **527**, 12219–12231 (2024).
- [33] Medin, Z. & Lai, D. Condensed surfaces of magnetic neutron stars, thermal surface emission, and particle acceleration above pulsar polar caps. *MNRAS* **382**, 1833–1852 (2007).
- [34] Dinh Thi, H., Baring, M. G., Hu, K., Harding, A. K. & Barchas, J. A. Monte Carlo Simulations of Polarized Radiative Transfer in Neutron Star Atmospheres. *ApJ* **992**, 188 (2025).
- [35] Radhakrishnan, V. & Cooke, D. J. Magnetic Poles and the Polarization Structure of Pulsar Radiation. *Astrophysical Letters* **3**, 225 (1969).
- [36] Hu, K., Baring, M. G., Barchas, J. A. & Younes, G. Intensity and Polarization Characteristics of Extended Neutron Star Surface Regions. *ApJ* **928**, 82 (2022).
- [37] Barchas, J. A., Hu, K. & Baring, M. G. Polarized Radiation Transfer in Neutron Star Surface Layers. *MNRAS* **500**, 5369–5392 (2021).
- [38] Dinh Thi, H. *et al.* Pulsed, Polarized X-ray Emission from Neutron Star Surfaces: the Effects of Vacuum Birefringence in the Magnetosphere. *ApJ in press*. arXiv:2512.22978 (2026).
- [39] Thompson, C., Lyutikov, M. & Kulkarni, S. R. Electrodynamics of Magnetars:

- Implications for the Persistent X-Ray Emission and Spin-down of the Soft Gamma Repeaters and Anomalous X-Ray Pulsars. *ApJ* **574**, 332–355 (2002).
- [40] Chen, A. Y. & Beloborodov, A. M. Particle-in-Cell Simulations of the Twisted Magnetospheres of Magnetars. I. *ApJ* **844**, 133 (2017).
- [41] Marshall, H. L. *et al.* O’Dell, S. L., Gaskin, J. A. & Pareschi, G. (eds) *The Globe Orbiting Soft X-ray (GOSoX) polarimeter concept study*. (eds O’Dell, S. L., Gaskin, J. A. & Pareschi, G.) *Optics for EUV, X-Ray, and Gamma-Ray Astronomy X*, Vol. 11822 of *Society of Photo-Optical Instrumentation Engineers (SPIE) Conference Series*, 118220O (2021).
- [42] Weisskopf, M. C. *et al.* The Imaging X-Ray Polarimetry Explorer (IXPE): Pre-Launch. *Journal of Astronomical Telescopes, Instruments, and Systems* **8**, 026002 (2022).
- [43] Di Marco, A. *et al.* Handling the Background in IXPE Polarimetric Data. *AJ* **165**, 143 (2023).
- [44] Deller, A. T., Camilo, F., Reynolds, J. E. & Halpern, J. P. The Proper Motion of PSR J1550-5418 Measured with VLBI: A Second Magnetar Velocity Measurement. *ApJL* **748**, L1 (2012).
- [45] Luo, J. *et al.* PINT: High-precision pulsar timing analysis package (2019). [ascl:1902.007](https://arxiv.org/abs/1902.007).
- [46] Baldini, L. *et al.* ixpeobssim: A simulation and analysis framework for the imaging X-ray polarimetry explorer. *SoftwareX* **19**, 101194 (2022).
- [47] Hobbs, G. *et al.* An ultra-wide bandwidth (704 to 4 032 MHz) receiver for the Parkes radio telescope. *PASA* **37**, e012 (2020).
- [48] Hotan, A. W., van Straten, W. & Manchester, R. N. PSRCHIVE and PSRFITS: An Open Approach to Radio Pulsar Data Storage and Analysis. *PASA* **21**, 302–309 (2004).
- [49] van Straten, W., Demorest, P. & Osłowski, S. Pulsar Data Analysis with PSRCHIVE. *Astronomical Research and Technology* **9**, 237–256 (2012).
- [50] Lower, M. E., Shannon, R. M., Johnston, S. & Bailes, M. Spectropolarimetric Properties of Swift J1818.0-1607: A 1.4 s Radio Magnetar. *ApJL* **896**, L37 (2020).
- [51] Hobbs, G. B., Edwards, R. T. & Manchester, R. N. TEMPO2, a new pulsar-timing package - I. An overview. *MNRAS* **369**, 655–672 (2006).
- [52] Edwards, R. T., Hobbs, G. B. & Manchester, R. N. TEMPO2, a new pulsar timing package - II. The timing model and precision estimates. *MNRAS* **372**, 1549–1574 (2006).

- [53] Everett, J. E. & Weisberg, J. M. Emission Beam Geometry of Selected Pulsars Derived from Average Pulse Polarization Data. *ApJ* **553**, 341–357 (2001).
- [54] Wilms, J., Allen, A. & McCray, R. On the Absorption of X-Rays in the Interstellar Medium. *ApJ* **542**, 914–924 (2000).
- [55] Verner, D. A., Ferland, G. J., Korista, K. T. & Yakovlev, D. G. Atomic Data for Astrophysics. II. New Analytic FITS for Photoionization Cross Sections of Atoms and Ions. *ApJ* **465**, 487 (1996).
- [56] Taverna, R. *et al.* The long quest for vacuum birefringence in magnetars: 1E 1547.0-5408 and the elusive smoking gun. *arXiv e-prints* arXiv:2601.15452 (2026).
- [57] Everett, J. E. & Weisberg, J. M. Emission Beam Geometry of Selected Pulsars Derived from Average Pulse Polarization Data. *ApJ* **553**, 341–357 (2001).
- [58] Ashton, G. *et al.* BILBY: A User-friendly Bayesian Inference Library for Gravitational-wave Astronomy. *ApJs* **241**, 27 (2019).
- [59] Speagle, J. S. DYNESTY: a dynamic nested sampling package for estimating Bayesian posteriors and evidences. *MNRAS* **493**, 3132–3158 (2020).
- [60] Gil, J., Gronkowski, P. & Rudnicki, W. Geometry of the emission region of PSR 0950+08. *A&A* **132**, 312–316 (1984).
- [61] Rankin, J. M. Toward an Empirical Theory of Pulsar Emission. IV. Geometry of the Core Emission Region. *ApJ* **352**, 247 (1990).
- [62] Johnston, S. *et al.* The Thousand-Pulsar-Array programme on MeerKAT - XI. Application of the rotating vector model. *MNRAS* **520**, 4801–4814 (2023).
- [63] Lower, M. E., Johnston, S., Shannon, R. M., Bailes, M. & Camilo, F. The dynamic magnetosphere of Swift J1818.0-1607. *MNRAS* **502**, 127–139 (2021).
- [64] Desvignes, G. *et al.* A freely precessing magnetar following an X-ray outburst. *Nature Astronomy* **8**, 617–627 (2024).
- [65] Foreman-Mackey, D., Hogg, D. W., Lang, D. & Goodman, J. emcee: The MCMC Hammer. *Publications of the Astronomical Society of the Pacific* **125**, 306 (2013).
- [66] Doroshenko, V. *et al.* Determination of X-ray pulsar geometry with IXPE polarimetry. *Nature Astronomy* **6**, 1433–1443 (2022).
- [67] Naghizadeh-Khouei, J. & Clarke, D. On the statistical behaviour of the position angle of linear polarization. *A&A* **274**, 968 (1993).
- [68] González-Caniulef, D., Caiazzo, I. & Heyl, J. Unbinned likelihood analysis for X-ray polarization. *MNRAS* **519**, 5902–5912 (2023).

- [69] Hibschan, J. A. & Arons, J. Polarization Sweeps in Rotation-powered Pulsars. *ApJ* **546**, 382–393 (2001).
- [70] Tong, H., Wang, P. F., Wang, H. G. & Yan, Z. Rotating vector model for magnetars. *MNRAS* **502**, 1549–1556 (2021).
- [71] Heyl, J. S. & Shaviv, N. J. QED and the high polarization of the thermal radiation from neutron stars. *Physical Review D* **66**, 023002 (2002).
- [72] van Adelsberg, M. & Lai, D. Atmosphere models of magnetized neutron stars: QED effects, radiation spectra and polarization signals. *MNRAS* **373**, 1495–1522 (2006).
- [73] Lai, D. & Ho, W. C. G. Resonant Conversion of Photon Modes Due to Vacuum Polarization in a Magnetized Plasma: Implications for X-Ray Emission from Magnetars. *ApJ* **566**, 373–377 (2002).

# 1 Figures

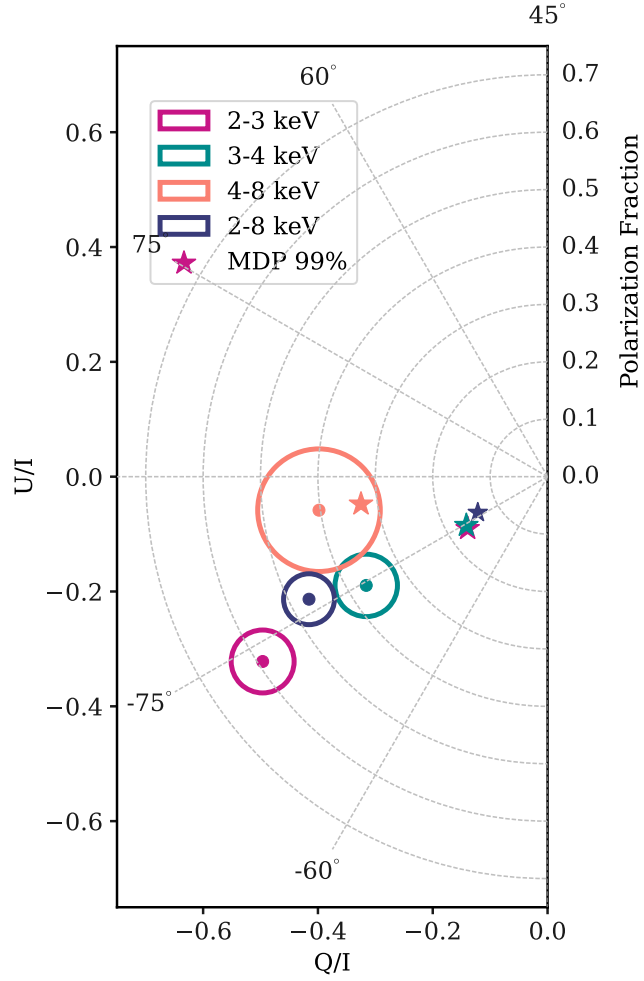


**Fig. 1** Background-subtracted and phase-averaged polarization measurements of 1E 1547.0–5408. We display the PD in 4 energy bands, 2–3, 3–4, 4–8, and 2–8 keV. Contours show the 68.3% ( $1\sigma$ ) confidence regions for Stokes  $Q/I$  and  $U/I$  (polarization degree and angle are shown in the radial and polar lines, respectively). The stars display the corresponding minimum detectable polarization at the 99% confidence level ( $MDP_{99}$ ) for each energy bin. The 2–8 keV energy-integrated polarization characteristics are shown in dark blue. Notably, the energy-integrated PD (dark blue) is 46% and the 2–3 keV PD (magenta) reaches 59%. The PD decreases substantially in the energy range 3–4 keV. The PD remains high at 40% in the 4–8 keV band, yet it suffers from a considerably lower signal-to-noise ratio (S/N). The PA does not exhibit strong variation across energy.

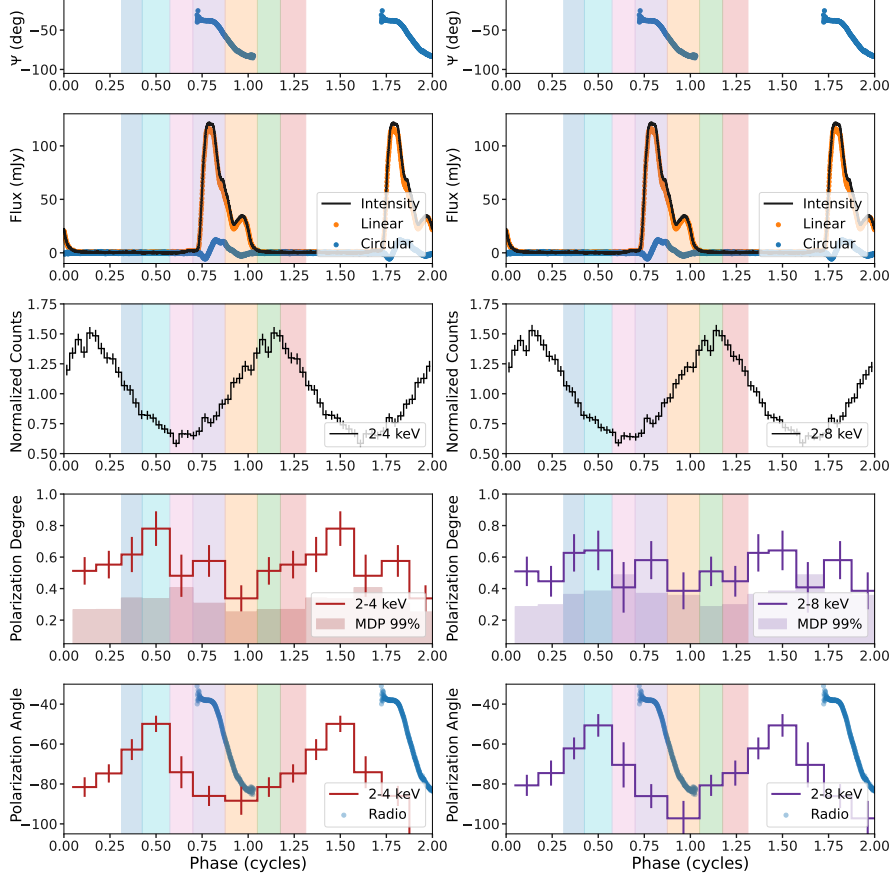


**Fig. 2** Phase-resolved radio and X-ray polarization characteristics of 1E 1547.0–5408. The uppermost row shows the radio polarization angle (two cycles shown for clarity). The second row displays the radio intensity curve (black) along with the total linear radio polarization (orange) as well as the circular radio polarization (blue). All of the shown radio data are averaged across our three Murriyang observations. The bottom three rows show the IXPE intensity, polarization degree, and polarization angle pulse profiles, respectively. The radio PA is also displayed in the bottom panel for ease of comparison to the X-ray PA. The IXPE pulse profiles are displayed according to two energy bands: 2–4 keV (left column) and 2–8 keV (right column). The shaded curves overlaying the polarization degree panels depict the MDP<sub>99</sub> at each corresponding phase bin. The vertical colored bands highlight the binning used for the IXPE phase-resolved polarization analysis.

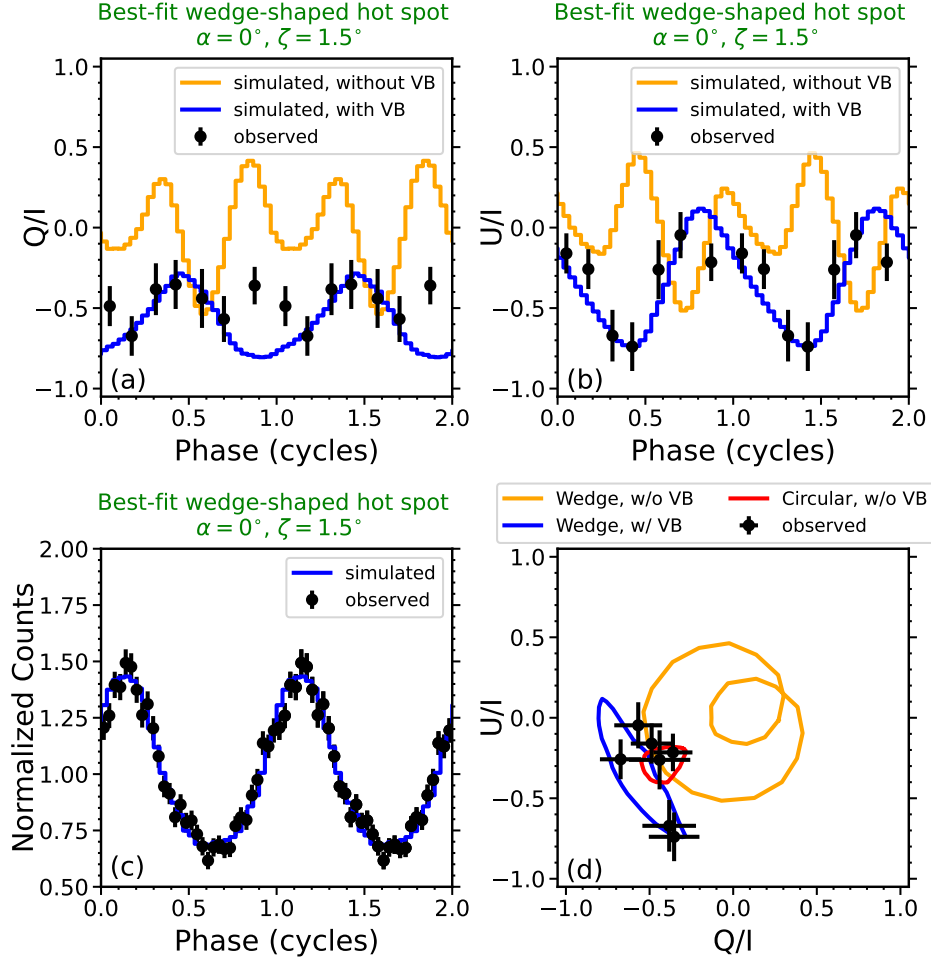


**Fig. 3** Simulated Stokes  $Q/I$  (panel a),  $U/I$  (panel b), and intensity (panel c) pulse profiles from *MAGTHOMSCATT* for a single hot spot wedge offset from the magnetic pole as a function of rotational phase (solid lines). The black dots represent the Stokes  $Q/I$  (panel a),  $U/I$  (panel b), and intensity (panel c) data extracted from IXPE in the 2–3 keV energy range. The case with the best statistical fit (lowest combined total  $\chi^2$ ; see Methods) incorporates vacuum birefringence, and corresponds to a magnetic colatitude of  $\theta_m = [0^\circ, 17^\circ]$  and longitude  $\phi_m = [0^\circ, 120^\circ]$  (zero longitude contains the rotation and magnetic axes); it is displayed in blue. The orange solid curves on the center and right panel show the corresponding polarization profiles wherein VB is turned off – these fits are statistically worse than those with VB on (see Methods). Panel (d) displays the comparison in the Stokes Q-U space between the observed data (black dots) and the simulated results obtained with the best-fit wedge-shaped hot spot with (blue line) and without (orange line) including magnetospheric VB, plotted for one rotational cycle. The red solid line represents the best result among the VB-off cases (see Methods), corresponding to a pole-centered circular hot spot with a magnetic inclination of  $\alpha = 2^\circ$  and a viewing angle of  $\zeta = 20.5^\circ$ .

## 2 Tables

**Table 1 Spectro-polarimetric model**

Model Parameter	Value $\pm 1\sigma$
$N_{\text{H}}$ ( $\text{cm}^{-2}$ )	$3.67 \times 10^{22}$ (fixed)
PD at 1 keV	$0.80 \pm 0.08$
PD <sub>slope</sub>	$0.15 \pm 0.02$
PA at 1 keV (deg)	$-67^{+4}_{-7}$
PA <sub>slope</sub> (deg/keV)	$-4 \pm 4$
BB kT (keV)	$0.720 \pm 0.005$
R <sup>2</sup> ( $\text{km}^2$ )	$1.07 \pm 0.05$
C <sub>NICER Obs 1</sub>	1.0 (fixed)
C <sub>NICER Obs 2</sub>	$1.08 \pm 0.05$
C <sub>NICER Obs 3</sub>	$1.05 \pm 0.05$
C <sub>NICER Obs 4</sub>	$1.01 \pm 0.05$
C <sub>DU1</sub>	$0.80 \pm 0.03$
C <sub>DU2</sub>	$0.80 \pm 0.03$
C <sub>DU3</sub>	$0.76 \pm 0.03$
Total Fit Statistic	1798.80 with 1511 d.o.f.

Spectral and polarimetric parameters for the best fit model, a single absorbed blackbody (BB) with linearly varying polarization. A multiplicative cross-calibration uncertainty is also added to the model. All uncertainties are calculated at the 68.3% confidence level ( $1\sigma$ ). The fit statistic employs a combination of the C-stat and Chi-Squared statistics used for NICER and IXPE, respectively. Blackbody emitting radius is derived adopting a distance of 4.5 kpc [31].

## 3 Methods

### 3.1 IXPE data reduction

The Imaging X-ray Polarimetry Explorer (IXPE), launched in December 2021, is the first imaging X-ray polarimetry space observatory. IXPE consists of three identical telescopes sensitive to 2–8 keV with detector units (DU) containing a Gas Pixel Detector (GPD) that images the photoelectron tracks from incoming X-rays [42]. IXPE observed the magnetar 1E 1547.0–5408 between UTC 2025-03-26T03:01:52 (MJD 60760.12629630) and UTC 2025-04-05T00:26:53 (MJD 60770.01866898) for a total livetime duration of 499.5 ks (see Table 3). We applied background rejection via the treatment recommended in [43] using the software *filter\_background.py*. No significant solar flaring or bursting activity was detected during this observation. The total number of counts detected in the full IXPE band is 20943. We performed the solar-system barycenter correction of the data using the HEASoft version 6.35 task `barycorr` according to the source J2000 coordinates,  $R.A = 237.725517^\circ$ ,  $Dec = -54.306697^\circ$  [44] with the JPL planetary ephemeris DE405. We subsequently used the pulsar timing package, PINT [45], to assign phases to each photon according to a phase-coherent timing solution that incorporated both radio and X-ray time of arrivals (ToAs) (see Extended Table 4 for details of the full timing solution).

After using DS9 to identify the peak of the centroid of the IXPE observation, we utilized the software `ixpeobssim` version 31.0.1 to perform data cleaning and extract high level data products, including spectra, lightcurves, and binned polarization cubes. The `ixpeobssim` task `xpradialprofiles` allowed us to examine the radial profiles and identify the extraction region size that optimized the data’s signal-to-noise ratio. Based on the radial profiles, we selected a circular source region of 0.5’ and an annular background with an inner radius of 2.5’ and outer radius of 4.5’. For the energy and phase-resolved products, we select the instrument response functions (IRFs) as `ixpe:obssim*:v13` from `ixpeobssim`’s pseudo-CALDB which provides the `arf`, `rmf`, `PSF`, `vignetting` functions, `modulation` factors, and `modulation` responses corresponding to the observation date [46]. For the spectral products, we generated the `arf` and `rmf` for each detector via the HEASoft tool `ixpecalcarf` and utilized the corresponding responses within Xspec during the spectral fitting. We verified that swapping the `ixpeobssim` `arf` and `rmf` curves with those built with HEASoft, or vice versa, returned consistent results.

The intensity X-ray pulse profiles are binned according to 32 equally spaced bins. The phase-resolved polarization degree and angle, on the other hand, were calculated according to 7 inhomogeneous phase bins to sample the morphology seen in both the radio and the X-ray intensity profiles.

### 3.2 NICER data reduction

The Neutron star Interior Composition Explorer (NICER) is a non-imaging soft X-ray telescope aboard the International Space Station sensitive between 0.2–12 keV with an effective collecting area of 1900 cm<sup>2</sup> peaking at 1.5 keV. Its superior timing

resolution of  $< 300$  nanoseconds makes NICER ideal for tracking magnetar temporal behavior. The data was extracted and cleaned using the HEASoft version 6.35 tool NICERDAS version 13a; the files were calibrated with NICER CALDB version 20240206. We applied standard filtering via the `nicer12` task. Each photon time of arrival was barycenter corrected to the solar system according to the JPL solar-system ephemeris DE405 using the HEASoft tool `barycorr`. We generated the lightcurves and spectra using the task `nicer13`, including the NICER spectral background model, SCORPEON which can be simultaneously fit with the source spectra to model sky and non-X-ray background contributions.

### 3.3 Parkes/*Murriyang* data reduction

We conducted three observations of 1E 1547.0–5408 concurrent to the IXPE campaign using *Murriyang*, the 64 m Parkes radio telescope, with the Ultra-Wideband Low (UWL) receiver system [47]. These observations were collected as part of the long-term Parkes Magnetar Monitoring Programme (project ID: P885). We recorded full Stokes pulsar fold-mode data using the MEDUSA signal processor, where the voltage stream was coherently de-dispersed at  $697 \text{ pc cm}^{-3}$  to correct for signal dispersion in the interstellar medium and then folded at the rotation period of the magnetar with 1024 phase bins covering each rotation of the magnetar. The data were subsequently averaged in time to form 30 s duration sub-integrations, each containing 3328 frequency channels covering the 704–4032 MHz band of the UWL. The start and end times and duration of each observation are listed in Table 3. We only made use of the data above 2.5 GHz in this work, as multi-path propagation through the interstellar medium induces substantial scatter broadening of the pulse profile below this cutoff frequency, resulting in a smearing of the phase-dependent polarization properties [27]. Radio-frequency interference from artificial sources were excised from the data by flagging and zero-weighting the contaminated frequency channels using the `paz` and `pazi` tools in `psrchive` to first remove known persistently affected channels, and then manually flag any remaining interference [48, 49]. The data were then polarization and flux calibrated following the procedure outlined in Ref. [50] using the full receiver model implemented in the `pac` tool of `psrchive`. Prior to each magnetar observation, we conducted a short, 80 s duration off-source pointing where a linearly polarized switched noise diode of known brightness was injected into the data stream. This was then compared to on/off observations of the calibration source PKS B1934–638 to determine the absolute gain and phase corrections. The polarimetric response of the instrument as a function of parallactic angle was corrected for using a model derived from a rise-to-set track of the bright millisecond pulsar PSR J0437–4725. We then corrected for the effects of Faraday rotation in the Stokes  $Q$  and  $U$  data due to propagation in the magnetized interstellar medium by applying the known rotation measure of  $-1847.6 \text{ rad m}^{-2}$  using the `pam` tool with the `--aux_rm` flag to de-rotate the data to infinite frequency.

### 3.4 Phase-coherent timing analysis

We obtained ToAs from the radio data by cross-correlating the individual frequency-averaged sub-integrations from each observation with a noise-free template via the

Fourier-domain Monte Carlo method implemented in the `pac` tool in `psrchive`. The profile template was generated from a set of von Mises functions that were fit to a fully time/frequency averaged copy of the first Murriyang total intensity profile via the `paas` tool. We derived X-ray ToAs from the IXPE and NICER data utilizing the Code for Rotational-analysis of Isolated Magnetars and Pulsars (`CRIMP`). We create an X-ray pulse template from a high S/N NICER profile, which was then fit to a sinusoidal function including only the fundamental harmonic; adding more harmonics did not improve the quality of the fit. We then merge each instrument’s event files, and split them into time intervals which incorporate 2000 counts and 4000 counts for NICER and IXPE, respectively, ensuring that each interval is  $\lesssim 0.5$  days. Finally, we fit the template to the phase-folded X-ray profiles of each interval, fixing all template parameters except for a phase-shift (i.e., the ToA) and the unpulsed component (which could show mild variability in NICER due to its non-negligible background).

An initial phase-coherent timing solution spanning the IXPE observing campaign was derived from the joint NICER and IXPE X-ray ToAs. We then used the `tempo2` pulsar timing package [51, 52] to refine this solution by re-fitting the magnetar spin frequency and spin-down rate while including the radio ToAs, thereby obtaining a locally phase-coherent timing model covering both the radio and X-ray observations. All ToAs were barycentered using the JPL planetary ephemeris DE405. We verified that both epoch-to-epoch and intra-observation variations in the radio pulse profile had a negligible impact on the final timing precision.

To ensure accurate absolute phase alignment between the radio and X-ray data sets, the final timing solution presented in Table 4 was obtained by fitting only the radio ToAs. This ensures that the rotational parameters are properly referenced to TZRMJD, which defines the phase zero-point of the radio profile template used to derive the radio ToAs, along with the associated phase-defining parameters TZRFRQ and TZRSITE. The NICER and IXPE X-ray data were then folded using this final timing solution with PINT [45].

We aligned the three Murriyang observations in phase using the above timing solution, and then averaged all three together in time and frequency to form a single, average polarization profile. The total linear polarization was computed as the quadrature sum of the Stokes  $Q$  and  $U$  profiles as  $L = \sqrt{Q^2 + U^2}$ , which was subsequently de-biased using the method outlined in [53].

### 3.5 X-ray Spectro-polarimetric Analysis

We performed spectro-polarimetric analysis of the 0.5–12 keV NICER and 2–8 keV IXPE spectral data using Xspec version 12.15.0 to gain insights into the nature of the source emission. For the NICER spectra, we grouped each spectral bin with a minimum of 5 counts per bin and used the  $W$ -statistic (`c-stat` within Xspec) for our statistical fitting. For the IXPE spectra, we grouped each spectral bin according to a minimum of 30 counts per bin and used the chi-squared statistics. In practice, the vast majority of energy channels contained substantially more counts than these minimum thresholds; the adopted grouping primarily ensures that the lowest and highest energy bins remain in the appropriate statistical regime for each instrument. Given the source’s low S/N at the low-energy bands ( $< 2$  keV), we froze the column density ( $N_{\text{H}}$ ) to a value

of  $3.67 \times 10^{22} \text{ cm}^{-2}$  as reported by Ref. [25]; we additionally used the Wilm solar abundances [54] along with the Verner cross-sections [55] to preserve consistency with the previous analysis. Finally, in the spectral models we impose a calibration constant between each telescope to track the calibration uncertainties during the observation (see Table 1).

We simultaneously fit the NICER SCORPEON background model with the source spectra. During the fits, we froze the normalization of the trapped electron components to 0 since they did not produce any significant contributions to the fitted background. The background models reveal that the NICER source spectra is dominated by the background below  $\approx 1.4 \text{ keV}$  and above  $\approx 7 \text{ keV}$  (see Extended Figure). Likewise, the IXPE spectra are background dominated above  $\approx 6 \text{ keV}$ , limiting the statistics of the higher energy contributions.

Historically, the broadband spectrum has been well described using either a 2BB+PL or a BB+2PL fit [24, 25]. However, due to the constrained energies at which the source is detectable in this data set, these spectra do not significantly capture the hot BB and/or PLs which appear at energies  $\gtrsim 6 \text{ keV}$ . We attempted to fit both a single and double BB model and performed an F-test to assess the inclusion of the second BB. We found an F-statistic value of 2.47 and the associated probability as 0.09. While the F-test indicates that including the extra BB component parameter could be reasonable, the 2BB best fit model does not yield physically reasonable values and thus we reject the extra component. Therefore we find that a single absorbed BB is sufficient to accurately describe the spectral shape of this particular data set, with a fit statistic of 1798.80 for 1511 d.o.f. Additionally, we find that applying a linear polarization component to the model performs the best with a total fit statistic of 1798.80 for 1511 d.o.f. compared to 1946.38 for a power-law component and 1840.09 for a constant component for 1513 d.o.f. Fitting a single absorbed power-law model yields largely unphysical parameters and thus this model was rejected.

Additionally, we note that while a significant detection was found in 4–8 keV band of the model-independent analysis (Figure 1), the high-energy component possesses large uncertainties, making it difficult to compare its behavior to the 2–3 and 3–4 keV and to ascertain any trend in the energy-resolved polarization characteristics overall. We further investigated the high-energy component by subdividing the energy bands to 4–5 keV and 5–8 keV, similar to the analysis presented in [56]. We analyzed these bins comparatively using a model-independent approach in `ixpeobssim` and a model-dependent approach in Xspec wherein each energy bin was fit according to an absorbed BB model with a constant polarization component. We fixed the BB model parameters to their best-fit value obtained from the energy-integrated NICER+IXPE spectral fits. This bin-by-bin spectro-polarimetric approach is standard practice in IXPE analyses and effectively yields model-independent polarization measurements. The Xspec error contours were obtained by performing a Monte Carlo sampling of the Xspec best-fit parameter confidence levels and converting the distributions into Stokes Q and U space. The results are presented in Figure 4. The `ixpeobssim` and Xspec analyses yield a PD of approximately  $50 \pm 10\%$  and  $48 \pm 15\%$  respectively, and the `ixpeobssim` analysis reveals that the 4–5 keV band exhibits a statistically significant detection at the  $\sim 5.5\sigma$  level. While these values appear to deviate from

the trend seen in the lower energy bands, the large uncertainties do not exclude the 4–5 keV band from being consistent with both the 2–3 keV and the 3–4 keV range. In this observation, the 4–8 keV band is comprised of 10% of the total counts, and the statistics between 2–4 keV dominate over those of the higher energy component. This may elucidate why the linear polarization model fits the 2–8 keV data well. A deeper exposure is required to constrain the data above 5 keV, where there may likely be a contribution from another spectral component [24, 25].

We use the Goodman-Weare MCMC method within Xspec with 10 walkers drawn from a multidimensional gaussian with means centered at the best fit model parameters. The MCMC generated three sets of 50000 simulated spectral fits for a total length of 150000. The first 5000 from each run were then burned. These runs were used to generate corner plots of the one- and two-dimensional posterior distributions to assess the correlations between the fitted parameters, shown in Extended Figure 7. We used the standard uniform priors implemented by Xspec for each model parameter. These priors were sufficiently large to sample the full physically-motivated parameter space, with an exception for the PA slope in which we expanded the prior limits from  $\pm 5^\circ/\text{keV}$  to  $\pm 30^\circ/\text{keV}$ .

### 3.6 Radio Polarization Analysis

Under the assumption that the radio emission from 1E 1547.0–5408 originates from above the polar cap of an approximately dipole magnetic field component [e.g., 28], we can use the rotating vector model of Ref. [35] to constrain the magnetic and viewing geometry of the magnetar. The linear polarization angle can be described as an S-shaped sweep across the profile as

$$\tan(\psi - \psi_0) = \frac{\sin \alpha \sin(\phi - \phi_0)}{\sin \zeta \cos \alpha - \cos \zeta \sin \alpha \cos(\phi - \phi_0)}, \quad (1)$$

where  $\psi_0$  is the reference PA at the inflection point of the RVM swing,  $\phi$  is the rotation phase of the magnetar,  $\phi_0$  is the pulse phase at which the PA inflection point occurs,  $\alpha$  is the magnetic inclination angle and  $\zeta = \alpha + \beta$  is the viewing angle between the spin-axis and our line of sight, which is in turn the product of the magnetic inclination angle and magnetic impact parameter ( $\beta$ ). Note that in the observer reference frame, the PA swing of the RVM is inverted, i.e.  $\psi_{\text{obs}} = -\psi_{\text{RVM}}$  [57]. We fit the RVM to the average profile obtained from combining our three concurrent *Murriyang* observations, where we sampled the model parameters using the `bilby` Bayesian inference library [58] as an interface to the `dynesty` nested sampling algorithm [59]. This was performed using a Gaussian likelihood of the form

$$\mathcal{L}(d|\theta) = \prod_i^n \frac{1}{\sqrt{2\pi\sigma_i^2}} \exp \left[ -\frac{(d_i - \mu(\theta))^2}{2\sigma^2} \right], \quad (2)$$

where  $d$  is the data (corresponding to the PA),  $\mu(\theta)$  is the RVM with model parameters given by  $\theta$ , and  $\sigma$  is the uncertainty on the PA. Note, we modified the formal uncertainties on the PA by adding in an additional error in quadrature term (EQUAD)

as  $\sigma^2 = \sigma_\psi^2 + \sigma_{\text{EQUAD}}$  to account for potential underestimation of the PA uncertainties due to uncorrected systematic effects. We assumed priors on  $\alpha$  and  $\zeta$  that were uniform in solid angle, i.e where  $(\pi(\theta) \propto \sin \theta)$ . Standard uniform priors were used for  $\phi_0$  and  $\psi_0$ . Our prior bounds for each parameter were set between  $0^\circ < \pi(\alpha) < 180^\circ$ ,  $0^\circ < \pi(\zeta) < 180^\circ$ ,  $270^\circ < \pi(\phi_0) < 360^\circ$  and  $-90^\circ < \pi(\psi_0) < 0^\circ$ . The resulting one- and two-dimensional posterior distributions are displayed in Extended Data Figure 8.

Our recovered values of  $\alpha = 3.4^{+1.3}_{-1.2}$  and  $\zeta = 7.5^{+3.0}_{-2.6}$  (equating to  $\beta = 4.2^{+1.7}_{-1.5}$ ) indicate 1E 1547.0–5408 is an aligned rotator, viewed almost pole-on. This geometry is seemingly in tension with the previously reported values of  $\alpha = 160^\circ$  and  $\beta = 14^\circ$  from Ref. [27]. However, this can be largely explained by a covariance between the magnetic and viewing angles due to the unknown spin direction of the magnetar, and a potential usage of the incorrect PA sign convention in their RVM fit (i.e  $\psi_{\text{obs}} = \psi_{\text{RVM}}$ ). Applying our more modern Bayesian inference based approach to fitting the PA swing of the 2007 observation analyzed by Ref. [27], we obtained values of  $\alpha = 10.2^{+3.9}_{-3.5}$  and  $\zeta = 17.7^{+6.7}_{-6.1}$ , for a magnetic impact angle of  $\beta = 7.5^{+2.9}_{-2.6}$ . This updated fit is consistent with our 2025 measurement to within the 68–95% confidence intervals. When the incorrect PA sign convention is used, we obtain similarly large values of  $\alpha = 169.7^{+3.5}_{-4.0}$  and  $\zeta = 162.2^{+6.1}_{-7.0}$  to those of Ref. [27].

An estimate of the radio emission height can be inferred from a combination of the profile width ( $W$ ) and the measured magnetic/viewing geometry. Assuming a filled emission cone, the beam-opening angle ( $\rho$ ) can be computed as [60]

$$\cos \rho = \cos \alpha \sin \zeta + \sin \alpha \sin \zeta \cos(W/2). \quad (3)$$

The opening angle is related to the emission height ( $h_{\text{em}}$ ) via [61]

$$\rho = 3\sqrt{\frac{\pi h_{\text{em}}}{2Pc}}, \quad (4)$$

where  $P$  is the magnetar rotation period and  $c$  is the vacuum speed of light. Typically the value of  $W$  is taken to be either the profile width at the 10% or 50% (i.e  $W_{10}$  or  $W_{50}$ ) levels. However, 1E 1547.0–5408 displays a clear, low-intensity precursor component in its radio profile that is not encompassed by either  $W_{10}$  or  $W_{50}$ , that if ignored would result in an underestimated beam opening angle, and by extension result in lower inferred emission heights of  $h_{\text{em}} = 473^{+447}_{-273}$  km and  $281^{+266}_{-162}$  km respectively. After iterating over different on-pulse window sizes, we settled on the 1.5% profile width of  $W = W_{1.5} = 142^\circ$ , which fully encompasses the entire radio profile (Fig 2 top panel). Substituting in this value, and our previous measurements of the magnetic inclination and viewing angles, we obtain  $h_{\text{em}} = 692^{+654}_{-400}$  km. This is broadly consistent with the bulk distribution of emission heights observed among the broader population of rotation-powered pulsars [62], but is substantially lower than other magnetars [63, 64].

### 3.7 X-ray Polarization Angle Modeling

As a counterpart to the radio RVM modeling, we model the X-ray PA swing using the RVM following the same formalism adopted for the radio analysis (Equation 1). The data are restricted to the 2–4 keV energy band, where the signal-to-noise ratio is highest and where the PA is energy-independent (see Figure 1), thereby minimizing systematic effects associated with spectral evolution.

We performed a Bayesian inference of the RVM parameters with the ensemble sampler `emcee` [65]. Following previous IXPE analyses of X-ray pulsars [e.g., 66], we used the wrapped-angle likelihood of [67]. This likelihood is specifically designed to handle the non-Gaussian uncertainties inherent to PA measurements and remains statistically valid in the presence of low-signal-to-noise data points. The phase-resolved PA profile is binned into 15 rotational bins. As with the radio RVM fits, we adopted isotropic, uninformative priors for the geometric parameters  $\alpha$  and  $\zeta$ , corresponding to uniform probability density in solid angle ( $\pi(\theta) \propto \sin \theta$ ), appropriate for randomly oriented axes. Uniform priors in angle space are assigned to  $\psi_0$  and  $\phi_0$ , with ranges  $-180^\circ < \pi(\psi_0) < 0^\circ$  and  $0^\circ < \pi(\phi_0) < 360^\circ$ .

The RVM provides an adequate description of the data, with  $\chi^2 = 12.8$  for 11 degrees of freedom ( $\chi^2_\nu = 1.16$ ). The resulting posterior distributions are shown in Figure 10. As expected given the lower photon statistics compared to the radio data, the X-ray constraints are broader, particularly for the viewing angle  $\zeta$  ( $\zeta = 69^{+25}_{-23}^\circ$ ; Figure 10). Nevertheless, the inferred geometric parameters are consistent with those obtained from the radio RVM fit at the  $2.5\sigma$  level. In particular, we recover a small magnetic inclination angle,  $\alpha = 18^\circ \pm 4^\circ$  (68% confidence interval), consistent with a quasi-aligned geometry. To assess the robustness of this result, we repeated the analysis using phase bins ranging from 8 to 16, obtaining consistent posterior distributions in all cases. We further validated our findings using an unbinned likelihood formalism [68], which yielded fully consistent parameter estimates.

We find a large and statistically significant difference between the X-ray fit for  $\phi_0$  and that in the radio; the offset amounts to  $\Delta\phi_0 \approx 80^\circ$  and may be attributed to several contributing factors. For uniform cone emission, the radio  $\phi_0$  marks the rotational phase at which the magnetic axis is closest to the line of sight, which arises at the meridional plane where the spin axis, magnetic axis and observer’s line of sight are coplanar. In contrast, the X-ray surface spot for, e.g., the wedge case is not uniform in magnetic longitude and with a centroid that is offset from the pole. Such an angular displacement between the X-ray and radio emission locales is forced by the phase lag in the respective intensity peaks. This then moves the X-ray  $\phi_0$  relative to the radio one. The  $\Delta\phi_0$  value likely receives an additional contribution from the distinct altitudes at which the polarization vectors are realized in the two wavebands. Our radio analysis suggests emission heights of order 50–100 stellar radii, whereas the polarization-limiting radius inferred for the X-ray emission likely lies at only a few tens of stellar radii (see Section 3.8 below). This difference will lead to some systematic shift in the inferred reference phase  $\phi_0$ , and could also be impacted by any toroidal twists to the field morphology at the respective altitudes.

The reference position angle  $\psi_0$  inferred from the X-ray RVM fit differs from the radio value by  $\approx 15^\circ$ , corresponding to a fractional difference of  $\lesssim 20\%$ . For a symmetric

radio cone, the parameter  $\psi_0$  corresponds to the projected orientation of the spin axis on the plane of the sky, modulo an additive constant associated with the dominant polarization eigenmode. For an ideal RVM in a pure dipole geometry, similar emission heights, and no propagation effects, the radio and X-ray reference PAs should either be identical if the two emissions are dominated by the same polarization mode (i.e., either both X-mode or both O-mode photons) or offset by  $90^\circ$  if they are not. The observed difference is modest enough to suggest that the radio and X rays are indeed dominated by the same polarization mode. It is likely that its non-zero value could be the imprint of magnetospheric field twists. The principal signature of twists is that they will rotate the PA (i.e., angle  $\psi_0$ ) due to the presence of a toroidal field component. Given somewhat distinct emission heights for the two wavebands, modest variance in PA is expected [69, 70]. At the same time, such twists are unlikely to impact the net polarization degree, since the PD is high due to the impact of VB.

In conclusion, the ability for the RVM to adequately describe the X-ray PA and the radio one provides an important consistency check for the VB interpretation. In the presence of strong QED birefringence, the X-ray polarization vector is expected to adiabatically track the local magnetic field direction out to the polarization-limiting radius, beyond which it becomes fixed. This naturally produces an RVM-like PA swing. The observed similarity between the X-ray and radio PA morphologies supports a scenario in which the large-scale dipolar field geometry, perhaps combined with a moderate contribution from twists, governs the polarization in both bands, with VB acting to preserve this imprint in the X-ray signal.

### 3.8 X-ray Emission Modeling Using *MAGTHOMSCATT*

The pulse profiles of soft X-ray intensities from NS provide powerful insights into the sizes and locations of hot spots on their surfaces, along with constraints on their geometric parameters, specifically the magnetic inclination  $\alpha$  of a dipolar field axis and the viewing angle  $\zeta$ , both relative to the rotation axis. For magnetars, the polarization measurements obtained with IXPE enable a new dimension in the analysis, both by providing tighter constraints on these parameters, yet also allowing probes of the exotic QED prediction of vacuum birefringence in strong magnetic fields. VB causes the polarization eigenmodes to decouple and rotate adiabatically with the magnetic field up to a certain distance from the surface (the polarization-limiting radius; [22]). Accordingly, the Stokes parameters observed at infinity are determined by the magnetic direction at that location. Without VB, the polarization properties at infinity depend on a convolution of the magnetic field directions on the stellar surface.

To model the anisotropy and polarization characteristics of X-ray emission observed for 1E 1547.0–5408 in order to constrain the hot spot locale and stellar geometric parameters, we employ *MAGTHOMSCATT*, a Monte Carlo simulation that treats polarized radiative transfer in magnetized NS atmospheres. The opacity is due to magnetic Thomson scattering, so that at any point on the surface removed from the magnetic pole, the  $\parallel$  or O-mode is the dominant polarization emergent from the atmosphere. Moreover, the radiation is strongly beamed along the magnetic field direction. The angular distributions of local anisotropy and polarization are detailed in Ref. [34]. The simulation tracks the complex electric field vector of each photon during

its atmospheric transport and magnetospheric propagation. As a result, the complete polarization information of the photon is captured, specifying the Stokes vector  $\mathbf{S} = (Q, U, V)$ , with  $V$  representing the circular polarization. General relativistic light bending and redshifting from the surface to infinity are included: herein we assume the NS mass and radius to be  $M_{\text{NS}} = 1.7M_{\odot}$  and  $R_{\text{NS}} = 12$  km, corresponding to a compactness of  $2GM_{\text{NS}}/(R_{\text{NS}}c^2) = 0.425$  (equivalent to that for  $M_{\text{NS}} = 1.44M_{\odot}$  and  $R_{\text{NS}} = 10$  km). The design, validation, and application of *MAGTHOMSCATT* are detailed in [34, 36–38].

The simulation is versatile in treating local atmospheric magnetic field directions, which in turn allows for modeling various hot spot configurations, that is, different shapes and locations. Surface atmospheric emissivities are uniformly distributed across a hot spot, and the intensity and polarization signals observed in a particular direction at infinity are obtained by integrating the intensity and Stokes parameters over all locales within a hot spot. We note that for photon energies well below the cyclotron energy, the anisotropy and polarization properties of emission from extended surface regions are almost independent of the photon energy [34], and therefore are expected to be insensitive to temperature stratification inside the atmosphere. The influences of QED VB on photon polarization during propagation through the magnetosphere can be switched on or off, as desired [38]. Other elements, such as mode conversion at the VR deeper in the atmosphere and field line twists in the magnetosphere, are not yet incorporated.

We performed a suite of simulations with a broad range of geometric parameters, to help examine the surface heat topology and viewing geometry of the system. In particular, we studied different hot spot configurations, which can be classified as either (1) a pole-centered circular hot spot, or (2) an offset hot spot. For the latter, we consider both circular and non-circular shapes. The inclination angle  $\alpha$  ranged from  $0^\circ$  (aligned rotator) to  $90^\circ$  (orthogonal rotator) in increments of  $2^\circ$ . The viewing angle  $\zeta$  ranged from  $0^\circ$  to  $180^\circ$ , divided into 180 bins, while the rotational phase  $\phi$  was divided into 30 bins per cycle. The Stokes parameters in the simulation are computed using coordinates connected to the spin axis and the line of sight, while the reference direction for the observed  $Q$  and  $U$  aligns with the celestial North. To account for this difference in coordinate directions, we introduce a parameter  $\Delta\phi_{\text{ref}}$ , ranging from  $0^\circ$  to  $180^\circ$  in steps of  $1^\circ$ . To constrain  $(\alpha, \zeta, \Delta\phi_{\text{ref}})$  and the hot-spot properties, we confronted the simulated intensity,  $Q/I$ , and  $U/I$  with the corresponding observed X-ray data. The resulting geometric parameters  $(\alpha, \zeta)$  are then compared with those derived independently from the radio analysis in Section 3.6. We note that the zero of phase,  $\phi = 0$ , in the observed pulse profiles (Figure 2) is arbitrary. Therefore, the intensity,  $Q/I$ , and  $U/I$  pulse profiles in the simulations are displaced in phase such that the position of the simulated X-ray intensity pulse peak coincides with that of the observed one.

The size of each hot spot matches the inferred BB emission region from the best spectral fit model (i.e.,  $A_{\text{BB}} = 13 \text{ km}^2 \approx 4\pi R_{\text{sp}}^2$ , with  $R_{\text{sp}}^2$  being the isotropic Stefan-Boltzmann law determination listed in Table 1 for a source distance of 4.5 kpc; here  $R_{\text{sp}}$  is the hot spot “radius”). This full-sky isotropic estimate is conventional in magnetar soft X-ray studies. For circular hot spots, the spherical cap area is

$A_{\text{BB}} = 2\pi R_{\text{NS}}^2 (1 - \cos[\theta_{\text{cap}}])$ , corresponding to a half-opening angle of  $\theta_{\text{cap}} \approx 10^\circ$ . For non-circular hot spots, we assume a wedge-shaped configuration of area  $A_{\text{BB}}$  for simplicity. The magnetic colatitudes spanned by each wedge extend from the pole out to a prescribed value ( $\theta_c = 0^\circ$ ), chosen to be between  $15^\circ$  and  $30^\circ$ ; the longitudinal range is then determined from the emission region area  $A_{\text{BB}}$ . In addition to these nominal cases with results presented below, we explored a variety of different  $\theta_{\text{cap}}$  and  $A_{\text{BB}}$  values, such that the area  $A$  of the hot spot ranges between  $A_{\text{BB}}/10 \lesssim A \lesssim 10A_{\text{BB}}$ , and found that the conclusion of the need for VB was not at all dependent on the choice of hot-spot area.

For emission from a pole-centered circular hot spot, scenarios with both  $\alpha$  and  $\zeta$  being small produce very low pulse fraction and, therefore, are disfavored by the intensity data. Moreover, if magnetospheric VB is inactive, the depolarization due to the cancellation of polarization vectors from different surface locales is significant when viewing over the pole. Therefore, we can expect that the radio inferred solutions,  $\alpha = 3.4^{+1.3}_{-1.2}$  and  $\zeta = 7.5^{+3.0}_{-2.6}$ , cannot reproduce the X-ray data, if the hot spot is a centered polar cap. Indeed, we find the best fit for this hot spot configuration is  $(\alpha, \zeta) = (2^\circ, 20.5^\circ)$  with the absence of VB (orange curves) being preferred, as shown in the top row in Figure 12. The intensity pulse fraction is slightly under-produced ( $\chi^2/\text{dof} = 49.9/30$ ), while the phase variation of the Stokes parameters is not well replicated, either with or without VB. Moreover, the viewing direction is inconsistent with the radio inferred value at the  $4\sigma$  level. Consequently, this hot spot scenario is unlikely. We note that this is the best fitting model within the full surveyed parameter space of system and hot-spot geometries, when VB is deliberately excluded.

The overall best-fit model to the observed pulse profiles of intensity,  $Q/I$ , and  $U/I$  in the 2–3 keV energy range specifically includes VB. This fit corresponds to a wedge-shaped hot spot of magnetic colatitudes extending from  $0^\circ$  to  $17^\circ$  and longitudes from  $0^\circ$  to  $120^\circ$  as shown in Figure 3. This model strongly favors the presence of VB, and results in  $\alpha = 0^\circ$  and  $\zeta = 1.5^\circ$  (intensity  $\chi^2/\text{dof} = 33.9/30$ , Stokes  $Q/I$   $\chi^2/\text{dof} = 19.0/4$ , and  $U/I$   $\chi^2/\text{dof} = 10.9/4$ ). The best-fit value for the coordinate rotation is  $\Delta\phi_{\text{ref}} = 105^\circ$ , corresponding to a position angle of the projected rotational axis measured  $75^\circ$  clockwise from the reference direction on the sky plane. For 1E 1547.0–5408, its polarization-limiting radius (PLR; where the two polarization modes recouple) is around 30 stellar radii for 2 keV photons at a viewing angle of around  $\zeta = 1.5^\circ$  in a dipolar field, according to Eq. (19) of [38], which is commensurate with the analysis of [71]. This geometry is broadly consistent with the configuration implied by the RVM best fit parameters for the radio emission. Moreover, the  $60^\circ$  magnetic longitude of its centroid is sufficiently offset from the meridian (longitude zero) that anchors the radio cone to accommodate the phase delay of the X-ray peak relative to the radio one. The case where VB is excluded exhibits strong oscillation due to the mixing of different magnetic field directions on the stellar surface as the star rotates, hence strongly disagreeing with the polarization data ( $\chi^2/\text{dof} = 106.8/4$  for  $Q/I$ , and  $\chi^2/\text{dof} = 95.6/4$  for  $U/I$ ; see the orange curves in Figure 3 and Figure 12).

We note that, while the model with VB in Figure 3 (blue curves), captures most of the data points in Stokes  $Q/I$  and  $U/I$  satisfactorily, the dominant contribution to the  $\chi^2$  values in these fits comes from the 7th phase bin at phase  $\phi = 0.875$ ,

which is only slightly above the 99% MDP. Therefore, at present, it is difficult to unambiguously identify the origin of this discrepancy. To improve the S/N around these phases, we explored different binning and found that the fits were improved, yielding  $\chi^2$  values of 11.4 and 4.4, respectively, for  $Q/I$  and  $U/I$ , with 3 dof. A second possible explanation is that our best-fit configuration represents the optimal solution within the explored parameter space, which was constrained in part by the radio geometry. Slightly different hot spot morphologies, particularly more complex or extended surface regions, could yield a marginally improved match to the profiles of the Stokes parameters. Nevertheless, introducing a more complex geometry would also naturally produce more structured  $Q/I$  and  $U/I$  curves in the absence of VB, and would therefore not alter our main conclusions for the requirement of magnetospheric VB. Future IXPE observations with higher S/N will allow us to better characterize these residuals and to reach a definitive conclusion.

A circular offset hot spot (with VB switched on) with its center located at colatitude  $\theta_c = 10^\circ$  and radius  $\theta_{\text{cap}} = 10^\circ$  (Figure 12, middle row) provides equally satisfactory results to the Stokes  $Q/I$  ( $\chi^2/\text{dof} = 18.1/4$ ) and  $U/I$  ( $\chi^2/\text{dof} = 9.4/4$ ) when compared to the wedge case. However, the intensity fit is of slightly lower quality ( $\chi^2/\text{dof} = 45.0/30$ ), leading to a higher combined total  $\chi^2$  value.

Finally, when considering the  $\alpha$  and  $\zeta$  as derived from the radio analysis, we find that a circular offset hot spot with its center located at colatitude  $\theta_c = 17.5^\circ$  and longitude  $\phi_c = 180^\circ$  provides satisfactory intensity fit ( $\chi^2/\text{dof} = 38.3/30$ ), yet the polarization degree is overestimated, with the magnitudes of both  $Q/I$  ( $\chi^2/\text{dof} = 47.8/4$ ) and  $U/I$  ( $\chi^2/\text{dof} = 62.9/4$ ) being too high at particular pulse phases, and underestimated at others (Figure 12, bottom row).

The conclusions drawn above were obtained for highly magnetized atmospheres where the emergent radiation is strongly beamed along magnetic field lines and highly linearly polarized mostly in the O-mode ( $\parallel$  polarization). The evidence in favor of VB persists even if the X-mode is dominant, as is the case in models with this state emerging from deep in the atmosphere. To verify this contention, we performed a set numerical experiments in which the polarization mode of each photon was switched upon its emergence from the surface, i.e.,  $X \leftrightarrow O$ . This change in photon polarization mode reverses the signs of Stokes  $Q$  and  $U$ , while leaving the beaming pattern unaffected. Given the geometric parameters inferred from the radio analysis, the observed high pulse fraction still strongly prefers an offset hotspot scenario. With this switch, the atmosphere is then X-mode-dominated, and the phase-resolved  $Q$  and  $U$  traces in the absence of VB also exhibit strong oscillations due to the rotation of the polarization vectors with local surface magnetic field vectors. This behavior is inconsistent with the observed behavior of the polarization PA, which exhibits only modest variations (see Figure 7). Consequently, VB is still required to reproduce the observed Stokes parameters. We found that, for the X-mode-dominated atmosphere, the inferred geometric angles are similar to those obtained for the O-mode-dominated atmosphere. Yet, the best-fit value for the coordinate rotation angle in this case is  $\Delta\phi_{\text{ref}} = 15^\circ$ , which differs by  $90^\circ$  from the O-mode result, as is intuitively expected when switching the polarization modes. We also performed simulations where the mode switching was only partial, and sometimes at modest depths inside the atmosphere, and for these,

the polarization degree of photons emergent from the atmosphere was always too low to explain the IXPE PD values.

The analysis on the observed X-ray PA data using an RVM, presented in Section 3.7, serves as an independent test for VB. In the presence of magnetospheric VB, one can show that the PA phase dependence of completely linearly polarized emergent radiation coincides with the azimuthal angle of the magnetic field direction at the polarization-limiting radius in the reference coordinates, see, e.g., [72]. Consequently, the X-ray PA only depends on the magnetospheric field geometry and should be consistent with the RVM given by Eq. (1), assuming a dipole configuration, and by extension with the geometrical elements derived from the radio RVM fits. For comparison, in Figure 13, we show the PA traces obtained from the wedge-shaped hot spot simulations for the best-fit geometry  $(\alpha, \zeta) = (0, 1.5^\circ)$  with and without including the VB effects in blue and orange, respectively. We note that the best-fit scenario shown in Figure 3 corresponds to a coordinate rotation of  $\Delta\phi_{\text{ref}} = 105^\circ$ . However, one can observe from the right panel that the simulated  $U/I$  trace (blue) slightly crosses zero at rotational phase  $\phi \sim 0.75$ , causing PA to switch sign. To avoid such discontinuity and obtain a better agreement with the observed PA, one can slightly shift  $\Delta\phi_{\text{ref}}$  from  $105^\circ$  to  $110^\circ$ . This shift only marginally degrades the quality of the fit for and  $U/I$ , while it does not affect the intensity result. Without VB, the strong oscillation exhibited in the Stokes parameters (see Figure 3) leads to a strong variation in the PA, as illustrated by the orange histograms in Figure 13, hence being strongly disfavored due to the observed PA. The PA trace obtained with VB (blue histograms) is consistent with the observed data in both 2–3 keV (black dots) and 2–4 keV (grey dots) bands.

Looking to the future, going beyond our magnetospheric focus, a broader indication of the action of VB in magnetars would be provided by detailed consideration of the VR in the atmosphere and its dependence on photon energy. This would need higher count statistics in the polarization data combined with increased spectral bandwidth (perhaps beyond 10 keV) so as to probe any extra components or departures from an approximate blackbody spectrum [24]. The VR energy at a given density is  $E_V(\rho) \simeq (1.02 \text{ keV}/B_{14})\sqrt{\rho Y_e}$  [73]. Assuming a hydrogen atmosphere ( $Y_e = 1$ ) and that the vacuum-plasma resonance layer lies at  $\rho \simeq 100\text{--}300 \text{ g cm}^{-3}$ , a typical range for magnetars [73], one finds that  $E_V \sim 3\text{--}5 \text{ keV}$  for 1E 1547.0–5408. The mode-mixing inherent in the VR physics naturally tends to depolarize the radiation emergent from the upper atmosphere, and there is some evidence for this in our IXPE dataset, namely in the 3–4 keV window in Figures 1 and 4. If VR influences within the atmosphere were significant below 3 keV, the ensuing depolarization of the surface signal would preclude being able to match the high PDs in the phase-resolved IXPE data regardless of whether or not VB was active in the magnetosphere. Note that it is also possible that partial absorption in a range of narrow proton cyclotron resonance energies (at 2.8 keV and below for  $B \lesssim 4.4 \times 10^{14} \text{ G}$  for 1E 1547.0–5408) could also impact the PD within the IXPE band; such a prospect motivates extensive simulation along the lines of theoretical studies of observed electron cyclotron features in accretion columns of X-ray binaries.

## 4 Extended Tables

**Table 2 Timing and Pulsar Parameters**

Pulsar parameters	
R. A. (J2000) <sup>a</sup>	15 <sup>h</sup> 50 <sup>m</sup> 54.124
Decl. (J2000) <sup>a</sup>	−54°18′24.11
$\nu$ (Hz)	0.477856(3)
$\dot{\nu}$ (s <sup>−2</sup> )	−4.(4) × 10 <sup>−12</sup>
Timing epoch (MJD TDB)	58350
Position epoch (MJD TDB)	54795
DM (pc cm <sup>−3</sup> )	697(1)
Time span (MJD)	60760–60770
Solar system ephemeris	DE405
TZRMJD	60764.7495
TZRFRQ	3275.71
TZRSITE	pks

Timing and pulsar parameters of the magnetar 1E 1547.0–5408 from our joint *Murriyang* + NICER observations

Note. Values in parentheses are the  $1\sigma$  uncertainties on the last digit. <sup>a</sup> Fixed to values from [44].

**Table 3 Observations**

Telescope	Observation ID	Start Date (UTC)	Stop Date (UTC)	Total Livetime GTI (ks)
IXPE	04003801	2025-03-26T03:01:52	2025-04-05T00:26:53	499.5
NICER	8020300101	2025-03-26T01:09:00	2025-03-26T15:13:00	1.057
NICER	8020300102	2025-03-27T01:51:01	2025-03-27T20:40:58	1.42
NICER	8020300103	2025-03-28T14:56:37	2025-03-28T22:47:32	1.051
NICER	8020300104	2025-03-31T06:33:41	2025-03-31T08:16:16	0.996
Murriyang	uwl_250326_173709	2025-03-26T17:37:09	2025-03-26T18:29:50	3.171
Murriyang	uwl_250330_171906	2025-03-30T17:19:06	2025-03-30T17:59:36	2.436
Murriyang	uwl_250331_131207	2025-03-31T13:12:07	2025-03-31T13:59:53	2.873

List of Parkes/Murriyang, IXPE, and NICER observation IDs, observation start and end times, and total livetimes used in this analysis.

## 5 Extended Figures

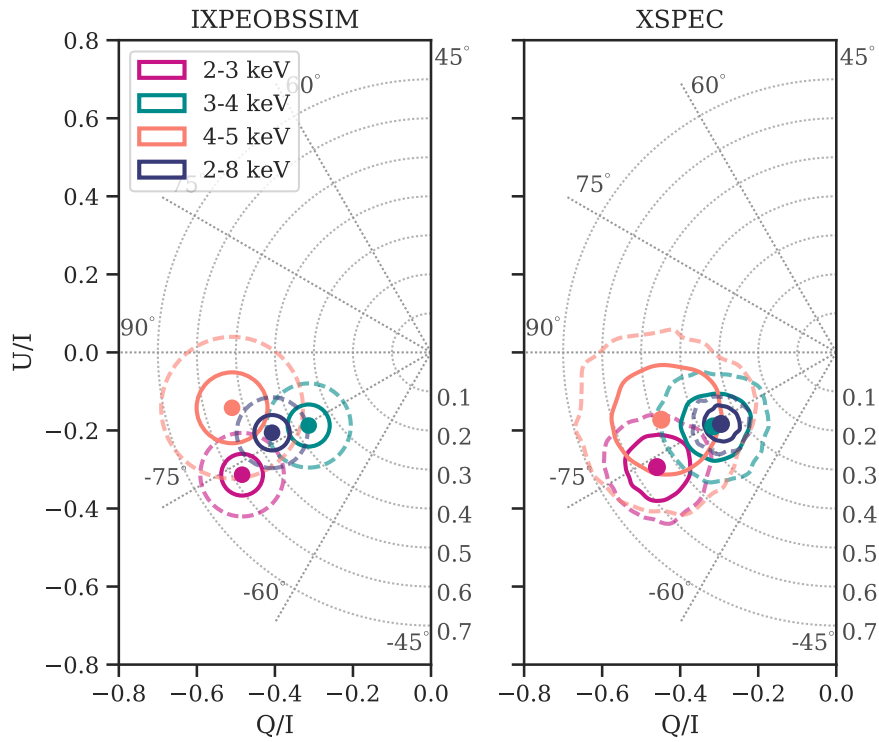


**Fig. 4** A comparative study between model-independent Stokes Q and U polarization characteristics obtained through using IXPEOBSSIM (left) and through applying a `polconst*bbbodyrad` spectral model in Xspec (right) at four energy bins: 2–3 keV, 3–4 keV, 4–5 keV, and 2–8 keV. The resulting PD and PA for the two methods are comparable to each other. Notably, both show a non-linear trend in the energy-dependence of the PD as the 4–5 keV band approaches the value of the 2–3 keV band at  $\sim 1\sigma$  level. Future observations with higher count statistics are needed to complement this study to more directly probe the nature of the high-energy polarization.

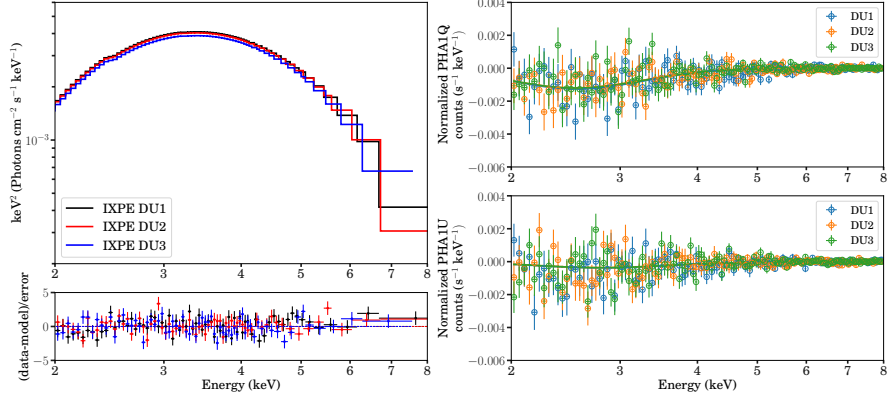


**Fig. 5** The simultaneous spectral  $\nu F_\nu$  models of the NICER+IXPE observations. The upper left panel displays the best fit model, a single absorbed blackbody with a linear polarization component: `constant*tbabs(pollin*tbodyrad)`. NB: Only the IXPE spectra are displayed here for the sake of visual clarity. The bottom left panel shows the data divided by the folded model for the absorbed BB model. The right-hand panels show the normalized Stokes  $Q/I$  (top) and  $U/I$  (bottom) spectra in linear space for the three IXPE DUs with the solid lines showing the best fit of the linear polarization component. The quasi-thermal BB is accompanied by a strong polarization signal that decreases as a function of energy.

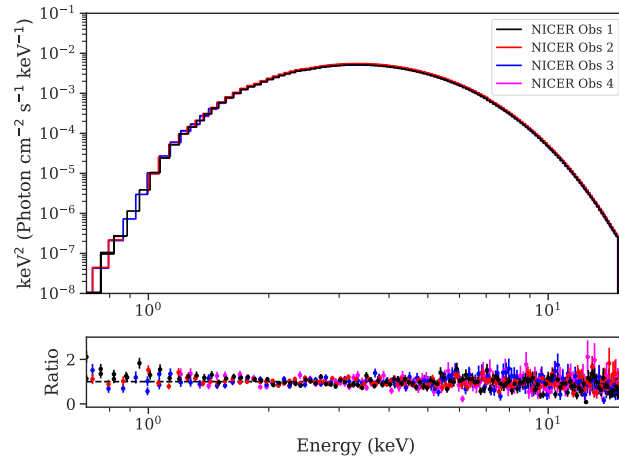


**Fig. 6** Simultaneous spectral modeling of the NICER+IXPE observations in the  $\nu F_\nu$  representation (see also Figure 5). The top panel shows the best-fit model to the NICER spectra, described by a single absorbed blackbody. For visual clarity, we do not display the SCORPEON background model components. The bottom panel shows the ratio of the NICER data to the folded model.

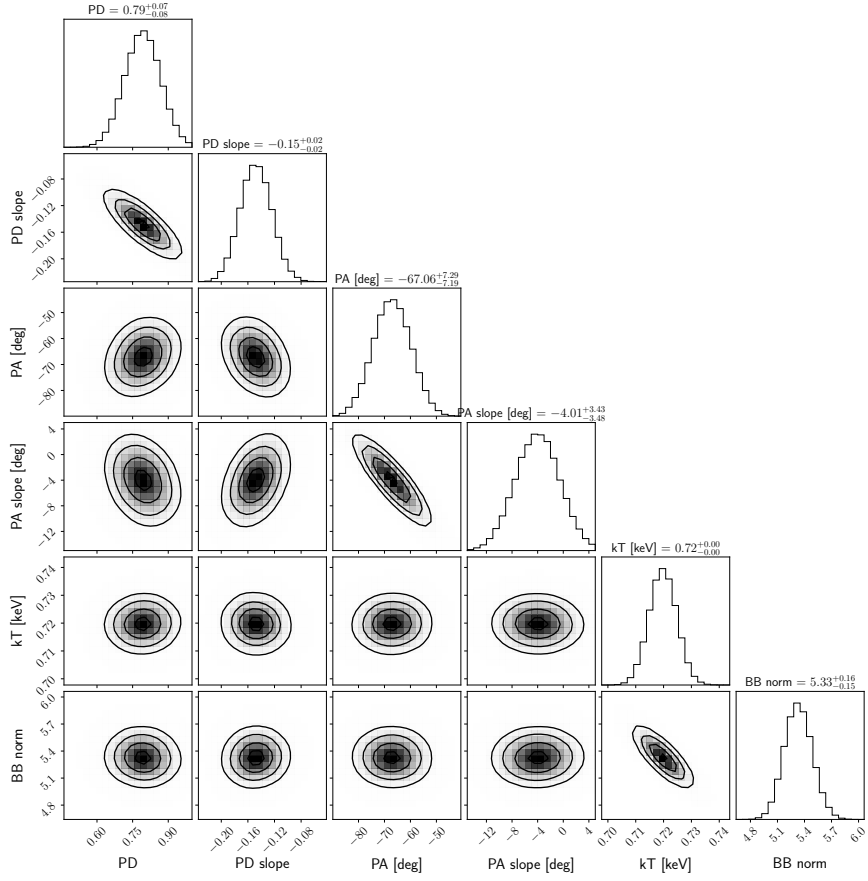


**Fig. 7** Corner plots of the one- and two-dimensional posterior distributions of the X-ray spectro-polarimetric parameters produced by an MCMC chain. The contours denote the 11.8%, 39.3%, 67.5%, 86.4% credible regions (corresponding to 0.5, 1, 1.5, and  $2\sigma$ ).

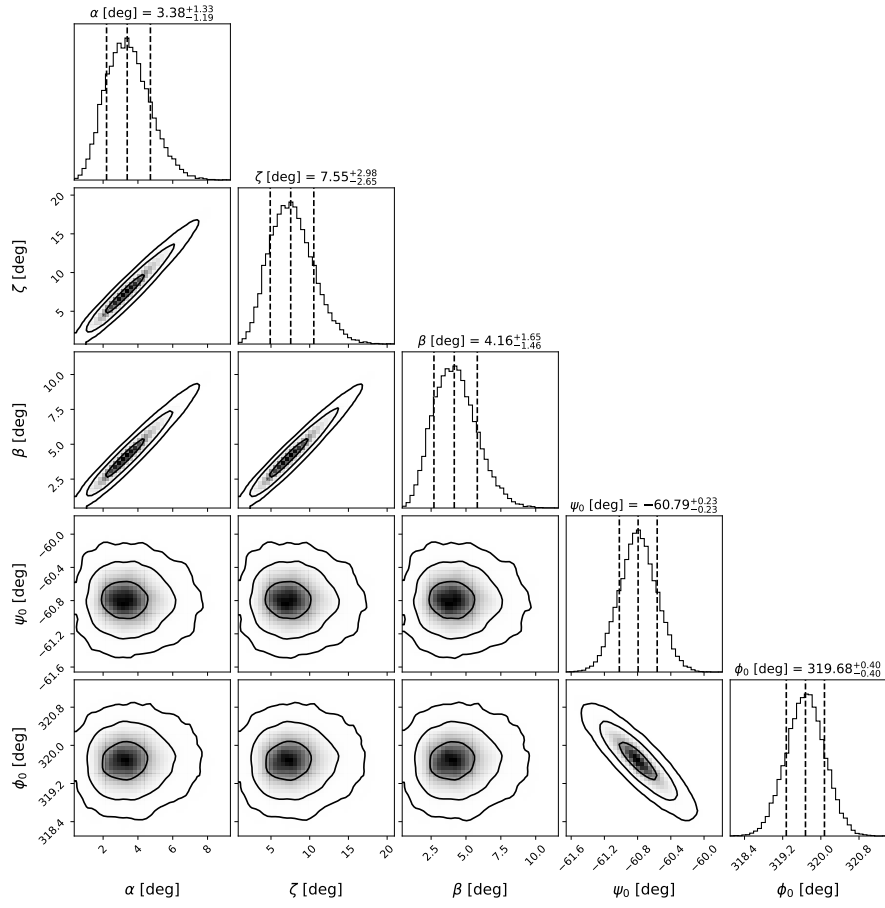


**Fig. 8** Corner plots of the one- and two-dimensional posterior distributions of the radio RVM fit parameters. The contours denote the 39%, 87%, and 99% credible regions (corresponding to 1, 2, and  $3\sigma$ ).

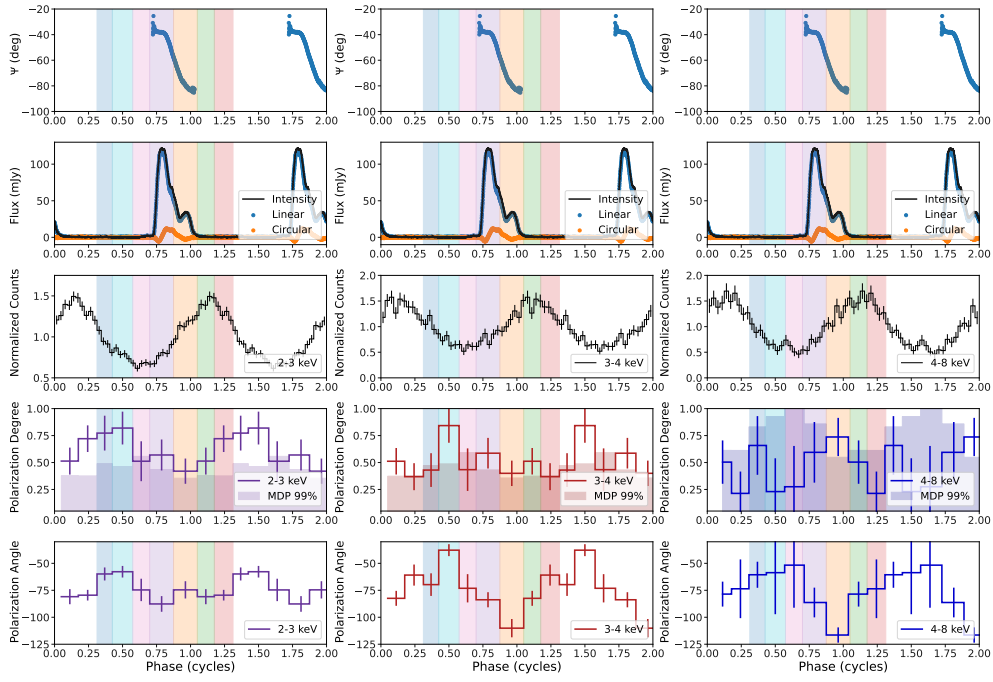


**Fig. 9** Complementary plot to Figure 2, with IXPE intensity, PD, and PA (shown in the lower three panels, respectively) binned according to 2–3 keV (left), 3–4 keV (center), and 4–8 keV (right).

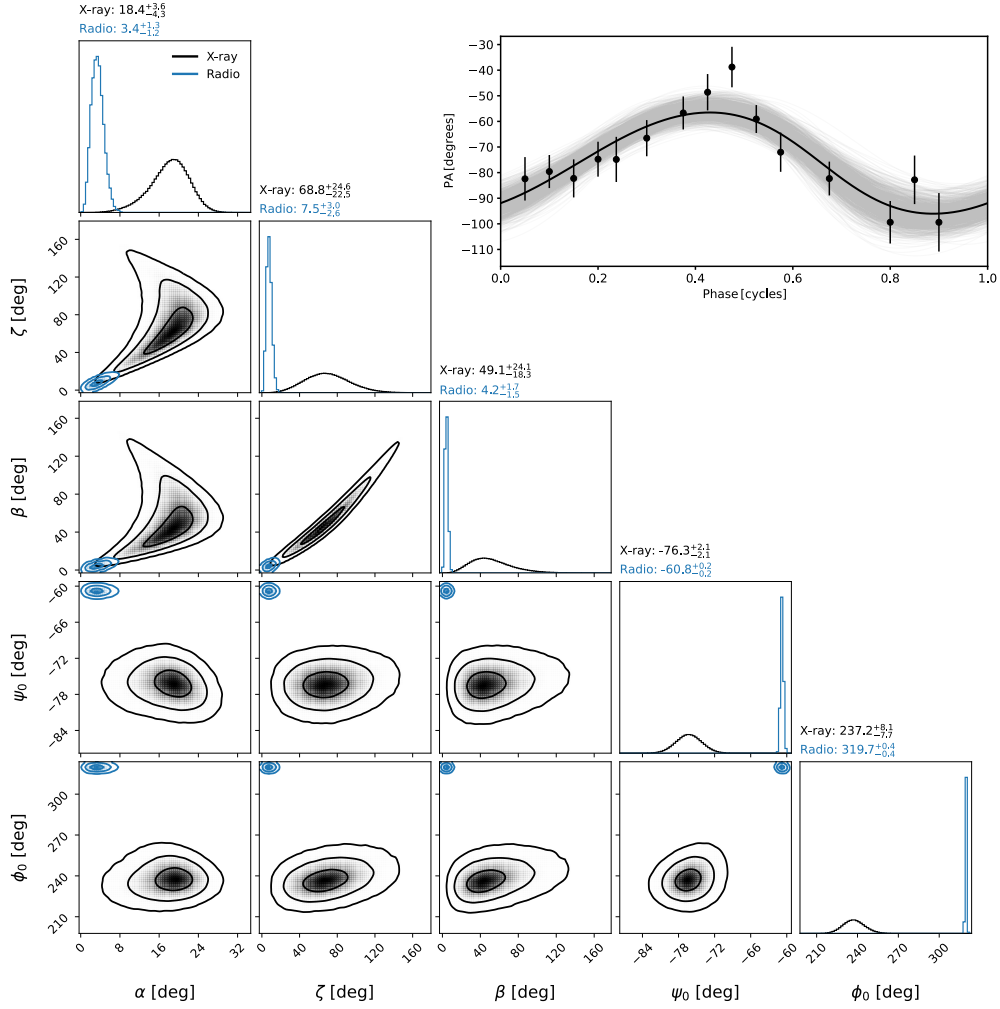


**Fig. 10** RVM fit to the phase-resolved X-ray PA. *Left panel:* Black contours represent the one- and two-dimensional posterior distributions for the RVM parameters  $\alpha$ ,  $\zeta$ ,  $\beta$ ,  $\psi_0$ , and  $\phi_0$ , obtained from a Bayesian fit to the 2-4 keV phase-resolved polarization angle profile using the [67] wrapped-angle likelihood. Contours denote the 39%, 87%, and 99% credible regions (corresponding to 1, 2, and  $3\sigma$ ). The blue contours are those derived from the radio RVM fit overlaid for ease of comparison. *Right panel:* Phase-resolved X-ray PA measurements (black points) overlaid with the maximum-posterior RVM model (solid black line). Light gray curves show random posterior draws, illustrating the range of model realizations consistent with the data.

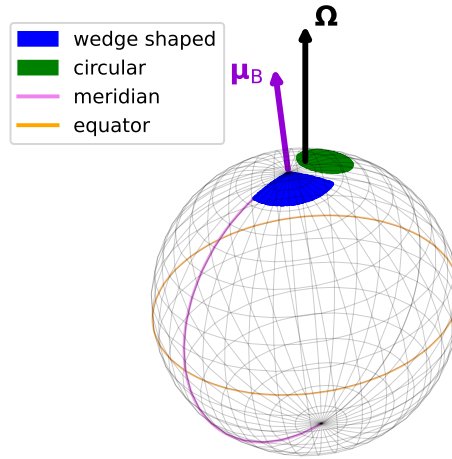


**Fig. 11** Illustration of a rotating NS with the magnetic axis  $\mu_B$  inclined from spin axis  $\Omega$ . The best-fit wedge-shaped hot spot and an offset circular spot, whose light curves are depicted in Figures 3 and 12 (bottom row), are depicted in blue and green, respectively. The violet (orange) curve indicates the meridian (equator) in magnetic coordinates. The radio cone is centered around  $\mu_B$ .

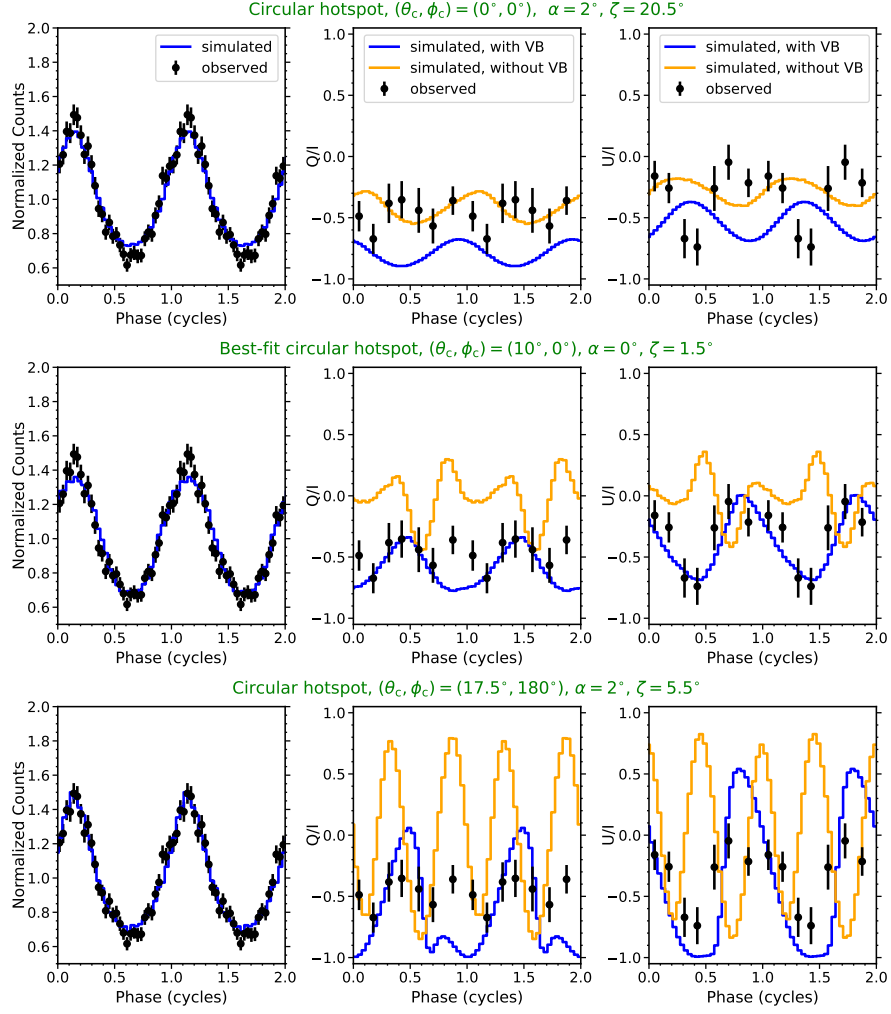


**Fig. 12** Simulated intensity (left column) and Stokes  $Q/I$  (center column) and  $U/I$  (right column) pulse profiles from *MAGTHOMSCATT* for a single hot spot offset from the magnetic pole as a function of rotational phase (solid lines) for three selected cases: pole-centered circular hot spot (top row), offset circular hot spot with its center located at  $(\theta_c, \phi_c) = (10^\circ, 0^\circ)$  (middle row), and offset circular hot spot with its center located at  $(\theta_c, \phi_c) = (17.5^\circ, 180^\circ)$  (bottom row). The inclination angle  $\alpha$  and viewing angle  $\zeta$  are indicated. The black dots represent data extracted from IXPE in the 2–3 keV energy range. The blue (orange) solid curves in each panel show the simulated profiles with (without) vacuum birefringence incorporated.

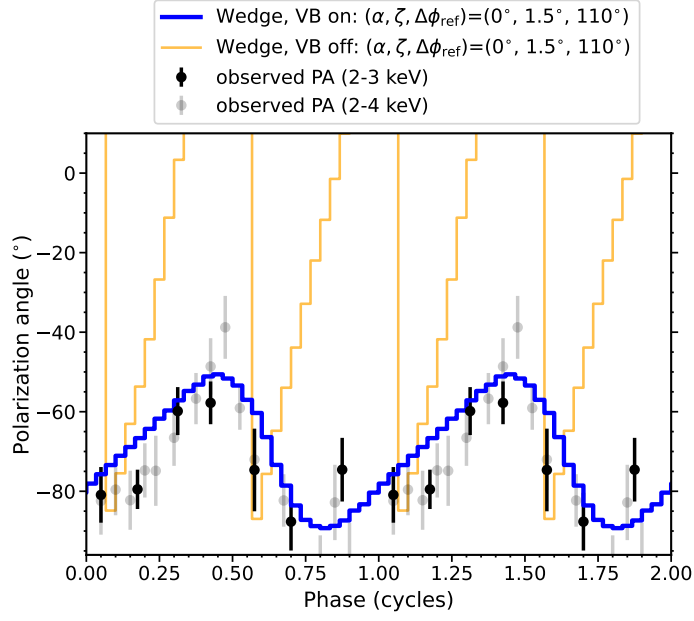


**Fig. 13** X-ray polarization angle as a function of rotation phase. The results from the simulation for the wedge-shaped hot spot with (without) VB effects are shown in blue (orange) for the best-fit geometry,  $(\alpha, \zeta) = (0, 1.5^\circ)$ . The black (grey) dots correspond to the X-ray PA data in the 2–3 (2–4) keV energy range. The RVM analysis of the PA light curve is presented in Figure 10.

## Declarations

**Acknowledgments.** This work reports observations obtained with the Imaging X-ray Polarimetry Explorer (IXPE), a joint US (NASA) and Italian (ASI) mission, led by Marshall Space Flight Center (MSFC). The research uses data products provided by the IXPE Science Operations Center (MSFC), using algorithms developed by the IXPE Collaboration (MSFC, Istituto Nazionale di Astrofisica - INAF, Istituto Nazionale di Fisica Nucleare - INFN, ASI Space Science Data Center - SSDC), and distributed by the High-Energy Astrophysics Science Archive Research Center (HEASARC). Murriyang, CSIRO's Parkes radio telescope, is part of the Australia Telescope National Facility (<https://ror.org/05qajvd42>) which is funded by the Australian Government for operation as a National Facility managed by CSIRO. We acknowledge the Wiradjuri people as the Traditional Owners of the Observatory site. This project was supported by resources and expertise provided by CSIRO IMT Scientific Computing, and made use of the Ngarrgu Tindebeek supercomputer at the OzSTAR national facility at Swinburne University of Technology. The OzSTAR program receives funding in part from the Astronomy National Collaborative Research Infrastructure Strategy (NCRIS) allocation provided by the Australian Government, and from the Victorian Higher Education State Investment Fund (VHESIF) provided by the Victorian Government. The material is based upon work supported by NASA under award number 80GSFC24M0006. G.Y. acknowledges NASA support under grants 80NSSC25K7257 and 80NSSC25K0283, through which R.E.S. and A.V.K. are partially supported. M.E.L. is supported by an Australian Research Council (ARC) Discovery Early Career Research Award DE250100508. M.G.B. thanks NASA for generous support under grants 80NSSC24K0589, 80NSSC25K7257 and 80NSSC25K0079. W.C.G.H. acknowledges support through grant 80NSSC23K0078 from NASA. J.B.C. acknowledges support under NASA award number 80GSFC21M0006. G.Y. acknowledges constructive discussion with Alexander Philippov on radio emission from magnetars, and Paul Ray on radio/X-ray timing analysis.

**Conflicts of interest.** The authors report no conflict of interest.

**Ethics approval and consent to participate.** Not applicable.

**Consent of publication.** Not applicable.

**Data availability.** NICER observations are readily accessible on the HEASARC data archive: <https://heasarc.gsfc.nasa.gov/W3Browse/nicer/nicermastr.html>. IXPE observations will be made publicly available on the HEASARC data archive following the expiration of the proprietary period: <https://heasarc.gsfc.nasa.gov/W3Browse/ixpe/ixmaster.html>. Radio observations made by *Murriyang* are publicly available from the CSIRO Data Access Portal (<https://data.csiro.au/>) following an 18 month proprietary period starting on the observation date.

**Materials availability.** Not applicable.

**Code availability.** Data reduction and analysis of X-ray products were performed using publicly available software Heasoft version 6.35.0 (<https://heasarc.gsfc.nasa.gov/docs/software/lheasoft/>) from the High Energy Astrophysics Science Archive

Research Center (HEASARC), particularly – FTOOLS v. 6.35.1, SAOImage DS9 v. 8.4b1, and Xspec v. 12.15.0. Generation and calibration of the NICER event lists was also performed by HEASoft’s NICERDAS version 12. The simulation and analysis framework ixpeobssim v. 31.1.0 was used to generate high-level IXPE data products: <https://ixpeobssim.readthedocs.io/en/latest/>. Additionally, the software filterbackground.py was used for treatment of the IXPE background, found here: <https://github.com/aledimarco/IXPE-background>. Timing analysis was performed using tempo2 (<https://github.com/mattpitkin/tempo2>), PINT (<https://github.com/nanograv/PINT>), and CRIMP (<https://github.com/georgeyounes/CRIMP/tree/main>). PyXspecCorner (<https://github.com/garciafederico/pyXspecCorner>) and corner.py (<https://corner.readthedocs.io/en/latest/>) was used to generate the X-ray spectro-polarimetric and radio RVM corner plots, respectively. Custom code for the *MAGTHOMSCATT* Monte Carlo simulation and the radio analysis are available upon reasonable request from corresponding authors.

**Author’s Contributions.** R.E.S. performed the X-ray polarization and spectral data analysis and contributed to writing the paper. H.D.T. and M.G.B. led the simulation analysis and theoretical interpretations and contributed to writing the paper. G.Y. is the principal investigator of the IXPE observation presented in this work, which was obtained through the NASA IXPE Guest Observer cycle 2 program. G.Y. performed the X-ray timing analysis and contributed to writing the paper. M.E.L. performed the radio observations and analysis, and contributed to writing the paper. M.N. provided support with the X-ray polarization analysis and contributed to writing the paper. F.C., J.B.C., A.K.H., W.C.G.H., C.P.H, P.K., P.S., A.V.K., and Z.W. provided comments and contributed to the writing of the paper. F.C. is the principal investigator of the Parkes P885 project.